THEORETICAL STUDIES OF THE RADAR PROPERTIES OF THE ICY GALILEAN MOONS OF JUPITER

FINAL REPORT
NASA GRANT NAGW-1964
JULY 1993

Principal Investigator
Von R. Eshleman
Center for Radar Astronomy
Electrical Engineering Department
Stanford University
Stanford, CA 94305–4055

Adapted from a PhD Dissertation
"Interpretation of Radar Data from the Icy Galilean Satellites and Triton"
By
Eric M. Gurrola
to be published in 1993

Abstract

The icy Galilean satellites of Jupiter—Europa, Ganymede, and Callisto—have unusual radar scattering properties compared with those of the terrestrial planets or Earth's Moon. There are three main features of the data that distinguish these targets: (1) The radar cross-section normalized by the geometrical cross-section is an order of magnitude larger than that of any terrestrial planet. (2) The reflected power is almost evenly distributed between two orthogonal polarizations with more power being returned in the same circular polarization as was transmitted whereas virtually all of the power returned from the terrestrial planets is contained in the opposite circular polarization to the one that was transmitted. (3) The echo power spectra have a broad shape indicating a nearly uniformly radar-bright surface in contrast to the spectra from the terrestrial planets that contain a strong quasi-specular component from the vicinity of the sub-radar point and very little reflected power from the rest of the surface. The normalized radar cross-sections decrease as the areal water-ice coverage decreases from Europa to Ganymede to Callisto. Recently, radar echoes from the polar caps of Mars and Mercury, and from Saturn's satellite Titan imply similarly strong cross-sections and have classically unexpected polarization properties and it is also thought that this is due to the presence of ice on the surface.

We analyze a model called the radar glory model and show that the main features of the radar echoes calculated from this model agree well with the observations from all three icy Galilean satellites. This model involves long radar paths in the ice below the surface and special structures in which the refractive index decreases abruptly at a hemispherical boundary. It is not known whether such structures exist or how they could be created, but possible scenarios can be imagined such as the formation of an impact crater followed by deposition of a frost layer follwed by a resurfacing event in which a layer of solid ice is placed above the layer of frost. Regardless of the exact geophysical processes required to create such structures, the superior ability of this model to account for all of the important observations with very few adjustable parameters and with no ad hoc assumptions is a compelling argument in support of at least the electromagnetic model. The key features of the electromagnetic model are multiple subsurface scattering events, total internal reflection, and a low degree of randomness imposed on a deterministic geometry that strongly favors backscattering.

Contents

List of Tables

List of Figures

Chapter 1

Introduction

The field of radar astronomy began shortly after World War II when radar echoes were obtained from Moon. (For a brief history of radar astronomy see Ostro (1987),Muhleman *et al.* (1965),and Muhleman *et al.* (1965).) In the following few decades before the echoes were obtained from the Galilean satellites, echoes were obtained from Mercury, Venus, Mars, Saturn's rings, and a few asteroids. The echoes from the terrestrial planets and Moon are similar and set the standard for what was expected from planetary targets. The typical echo from the terrestrial planets is characterized by a small radar cross-section relative to its geometrical cross section. When circularly polarized fields of a given helicity are transmitted nearly all of the reflected fields are in the opposite helicity state and the spectra (a plot of power versus Doppler frequency) show a strong quasi-specular component around the sub-radar point and a weak diffuse component from the rest of the surface.

The first attempt to detect radar echoes from the Galilean satellites was made in 1970 (Campbell *et al.*, 1977), but was not successful. In 1974 Ganymede became the first Galilean satellite detected by radar (Goldstein and Morris, 1975) using the 64 meter Goldstone antenna. From the very weak echoes obtained it was estimated that the radar cross section of Ganymede was 12% that of a perfectly conducting, smooth sphere—a result that was comparable with other radar targets such as the terrestrial planets and asteroids. These echoes also revealed a broad power spectrum which was quite different than that observed for the terrestrial planets, but comparable to the spectrum obtained from an asteroid's rough surface. This detection was of interest for the fact that it could be done, but did not hint at the truly unique nature of Ganymede's, as well as the other icy Galilean satellites', radar echoes. The entire set of Galilean satellites were observed using radar in 1975 using the Arecibo S-band radar system which had five times the sensitivity of any other system for studying the Galilean satellites (Campbell *et al.*, 1977). Since then, radar echoes from the Galilean satellites have been obtained whenever Jupiter was at declinations favorable for viewing by Arecibo (a period of about four years once every about eleven years). A summary of the observations made in the years 1975–1979 are given in Ostro (1982) and a summary of the observations made in the

years 1987–1991 are given in Ostro *et al.* (1992).

The radar echoes from the Galilean satellites are very different than those from the terrestrial planets and the term bizarre has often been used when referring to them. Soon after it was recognized that the echoes from these satellites were so unusual it was realized that the fact that the surfaces are made up of large quantities of water ice, which is a poor absorber of microwaves, had something to do with the observations. However, after more than almost two decades in which at least five serious models for explaining the data have been proposed the issue has not been settled to any degree of certainty. The basic reason for this is that the data do not sufficiently constrain the models. New types of data are required such as data from a bistatic radar experiment in which different antennas at different angular positions are used to transmit and receive the radio waves so that the angular dependence of the scattering can be determined.

In the following chapter we will give background information on the basic physical characteristics of these satellites, the properties of ice that are important to understanding the radar echoes, the experiment and the data, and the models that have been proposed to explain the data. Then in chapter 3 we present the details of our analysis of the radar glory model. This model was first proposed by Eshleman (1986) and this report extends the analysis of that model to include certain effects that were previously neglected and to calculate the Doppler spectra which had not been calculated before. That chapter will end with a comparison of model calculations with the data and it will be seen that the model predictions are consistent with all the main features in the data.

Chapter 2

Background

2.1 The Incidence and Importance of Ice

Four of the satellites of Jupiter are referred to as the Galilean satellites in honor of Galileo who is credited with their discovery in 1610 using one of the earliest telescopes. Of these four three of them—Europa, Ganymede, and Callisto—are different than the fourth one—Io—because their surfaces are largely composed of ice (throughout this document the term ice refers to H_2O ice, usually in its main crystalline form called ice Ih (Hobbs, 1974)). It is this distinguishing feature that is most likely responsible for the unusual radar backscattering properties of the three icy satellites that is the subject of this report. Io is a very interesting satellite, but it is not a very good radar backscatterer and so I will not discuss Io any further.

Some of the physical characteristics of the Icy Galilean satellites are summarized in Table 1. Europa is about the size of Earth's Moon and its bulk composition is mostly silicate rock material with a crust of ice to a depth of at least 25 km. Spectral measurements indicate that the surface of Europa is virtually 100% ice. Ganymede and Callisto are about the size of Mercury and their bulk composition is a mixture of ice and rock. Ganymede is a well differentiatied body and so much of the ice is contained in the upper layers. Spectral measurements indicate that Ganymede's surface is about 50% ice. Callisto on the other hand is not very well differentiated and so it does not have most of its ice near its surface. Spectral measurements indicate that its surface contains less ice than Ganymede and that the aerial coverage is about 10%. The temperatures of all these satellites is about 100 K.

Most of the theories that have been proposed to explain the strange backscattering properties of these satellites involves subsurface scattering and long radar paths. This is possible because ice at these cold temperatures is not a strong absorber at microwave wavelengths. Actually no laboratory measurements are available at these temperatures of the complex dielectric constant. It is usually assumed that the absorption length in ice on these satellites is much longer than what is required for

the particular model being analyzed. This assumption appears to be based on an extrapolation using the standard Debye theory of the permitivity with the temperature dependence of certain parameters determined from theory and measurements made at long wavelengths ($\lambda > 1.5$ km) and temperatures down to 200 K (Thompson and Squyres, 1990). However, Thompson and Squyres (1990) argue that this extrapolation is inaccurate at microwave frequencies because the Debye formulas don't account for the large tails of absorption features in the millimeter wavelength range that influence the microwave absorption. Thompson and Squyres derive formulas with empirically determined parameters based on measurements from optical wavelengths to 8.6 m-λ at temperatures above 213 K which they propose to be better than the previous formulas for extrapolating to cold temperatures at microwave frequencies. The real part of the dielectric constant given by the Thompson and Squyres formulas agrees with the previous results at all wavelengths and temperatures. However, the imaginary part of the dielectric constant in the Thompson and Squyres formulas is orders of magnitude larger than that previously reported. A convenient parameter for discussing absorption is the absorption coefficient which is proportional to the imaginary part of the dielectric constant and is the propagation distance required to reduce the power by a factor $1/e$. At 12.6 cm-λ and 100 K, the Thompson and Squyres formulas give an absorption length of 22 km whereas the older formulas give 9×10^{15} km. The absorption lengths at all temperatures of interest at the Galilean satellites based on the standard formulas are much larger than the radii of the satellites. This justifies the usual analyses that regard the ice to be free of absorption. However, if the Thompson and Squyres formulas are correct, then the absorption in the ice may play an important role in the differences in the observed scattering properties of these satellites. For future reference, the refractive index and absorption length based on the Thompson and Squyres formulas at temperatures of interest are tabulated in Table 2. In our analysis, we have neglected the effects of absorption by the ice like all the other theories. The effects of absorption can be accounted for in an *ad hoc* manner by multiplying the power by $\exp(-L/\alpha)$ where L is the total distance traveled in ice by the radar waves and α is the absorption length.

Table 3 shows the possible polymorphs of ice that could possibly exist on the icy Galilean satellites (Gaffney and Matson, 1980). The polymorphs are forms of ice other than the normal I_h hexagonal form of ice that form at higher pressures. Gaffney and Matson hypothesize that the polymorphs will occur when impacts occur during crater formation. They also expect that at the temperatures found in the outer solar system, that the I_c form is stable and will occur in abundance since there has been a long time for it to accumulate. A likely place to find this form, they claim, might be as a light frost cover in the low albedo regions of Ganymede poleward of 40° latitude.

Meteor bombardment, pressure, and thermal effects also act to modify the structure of ices on satellites (Smoluchowski and McWilliam, 1984). Meteor bombardment in porous ice results in some densification, but mainly results in the formation of ice crystalline polymorphs and in amorphous ice below 150 K. Smoluchowski (1983) discusses amorphous ice which is created when water vapor

condenses directly into ice at temperatures below about 150 K. Smoluchowski hypothesizes that there should be up to 50% of the ice layer at an impact site which is amorphous ice. Impacts of meteorites into ice may produce crystalline ice polymorphs in the crater; the ejecta will consist of both liquid and vapor; the liquid will partially evaporate and the rest will refreeze on the surface forming regular crystalline ice I_h; the vapor will partially escape from the planet and partly condense into amorphous ice on the solid ejecta and around the crater. Pressure densification, controlled by creep or slow plastic deformation and diffusion, is significant to depths of hundreds of kilometers because of the low temperatures involved. Thermal effects result in densification as well due to: 1) migration of pores toward warmer regions when thermal gradients exist; and 2) diffusion when isothermal conditions exist.

There doesn't appear to be much data on the dielectric properties of these other forms of ice, particularly at the cold temperatures of interest for the Galilean satellites, but it is likely that the dielectric constant is differnet and this may cause interesting inhomogeneities and discontinuities in the refractive index of the ice.

2.2 The Unusual Radar Backscattering Properties

Figure 1 schematically shows the geometry of a radar backscattering observation of the Galilean satellites using Arecibo. The optimal viewing times are at Jupiter opposition (when Jupiter, Earth and Sun are in alignment with Jupiter at its closest to Earth) when Jupiter is about 4 AU (astronomical units) from Earth. The round trip light time is a little over an hour. In each experimental "run" CW (continuous wave, meaning a sinusoidal wave that is unmodulated for a time very long compared to the period of oscillation) signals were transmitted for the duration of the round trip light time when the radar was switched to receive mode. Usually circularly polarized fields in one helicity state were transmitted and the fields in both helicity states were received. On a few occasions linear polarization in one particular orientation relative to the feed of the Arecibo antenna at transmit time were used and two orthogonal linear polarizations were received.

The use of CW signals permits a certain kind of mapping of the surface of a satellite as described in Green (1968) (see also Ostro (1987)). Figure 2 shows a satellite of radius R and spin frequency Ω in radians. A cartesian coordinate system with its Z axis pointing in the direction of Earth and with the XZ-plane containing the spin axis of the satellite is defined. Also shown is a scattering center located at spherical polar coordinates (R, Θ, Φ). If the incident fields are sinusoids of frequency ω_0, then the fields reflected from the scattering center will have a doppler shifted frequency. The Doppler shifts incurred in the signal received by the radar at Earth are due to many sources such as the orbital and rotational motions of the Earth, the orbital and rotational motions of the satellite, and other less important contributions such as Gravitational red and blue shifts. The radar system at Arecibo is programmed to remove the Doppler shifts due to Earth's motions and the orbital

motions of the satellite; these motions are known very accurately. The remaining Doppler shift is due to the spin of the satellite. If we call ω the frequency of the reflected fields after these known effects are removed, then it is a simple matter to calculate

$$\omega - \omega_0 = 2k_0 Y_s \Omega \sin \Psi$$

where $k_0 = \omega_0/c$ is the wavenumber of the incident fields and Y_s is the Y coordinate of the scattering center. From this formula we see that if we compute the Fourier spectrum of the signal that is received at Earth, then the power at frequency ω has contributions from all scatterers of the same Y coordinate across the surface of the satellite. Thus, if we look at the power at a single frequency it is as if we looked at the power reflected in a strip parallel to the plane containing the spin axis and the radar line of sight.

Another possible mode of operation of the radar that would provide a different sort of map would be to transmit short pulses. Then the power reflected at a given time before the arrival of another pulse is due to scattering centers located at the same colatitude Θ. Thus, this would provide a kind of map of the surface in terms of rings of constant colatitude. It is also possible to transmit sinusoidal signals that are modulated by short pulses which would then allow the power to be resolved in time and frequency. The power at a specified time and frequency would be from scattering centers at the intersection of a ring of constant Θ and a line of constant Y, that is, from two points on the surface. It turns out that it isn't possible to do this kind of mapping on the Galilean satellites as described here. The reason is that in order to prevent aliasing of the Fourier spectrum, the frequency of the pulses would have to be larger than the bandwidth of the reflected signals and in order to prevent a kind of aliasing in the time dispersed signal (to arrange it so that only one pulse is interacting with the surface of the satellite at a time) it is necessary that the time between the pulses be larger than the round trip travel time of a pulse from the sub-radar point (at $\Theta = 0$) to the terminator (at $\Theta = \pi/2$) and back. Thus, these two requirements place constraints on the time between the pulses, but the constraints are in opposite directions. If B is the bandwidth of the reflected signals and if T is the round trip time of a pulse across the surface and if τ is the time between pulses, then the two requirements are $1/\tau \geq B$ and $\tau \geq T$ which can be combined to one requirement for the combined type of mapping $1 \geq BT$. Assuming $\Psi = \pi/2$, then $B = 8\pi R/(\lambda_0 P)$ where $\lambda_0 = \omega_0/c$ is the wavelength of the incident fields and $P = 2\pi R/\Omega$ is the rotation period of the satellite and $T = 2R/c$. Table 3 tabulates B, T, and their product. From the table we see that the product BT is larger than unity in all cases except Callisto at 70 cm-λ which is not a good wavelength in terms of SNR; therefore, it is not possible to simultaneously map the surface in frequency and time delay. Radar targets for which BT is greater than unity are said to be overspread. All of the radar echoes from the Galilean satellites have been obtained using CW signals. Recently Hudson and Ostro (1990) developed a method to produce two dimensional maps of the surfaces of spherically symmetric targets using only Doppler shifted echoes from CW signals from several different rotation phases (that is, from several different runs of the experiment on different nights). The results of this

mapping procedure using the most recent Arecibo data are discussed in Ostro *et al.* (1992).

The analysis presented here deals with the basic mechanisms causing the unusual backscattering properties of these satellites. Therefore, I will not discuss mapping techniques or correlations between radar results and optical images.

Figure 3 shows a comparison between a typical radar echo from a terrestrial planet and from Europa. The main features of this spectrum from Europa is typical of what is also observed from Ganymede and Callisto and will serve for the purpose of this discussion as a typical spectrum from the Galilean satellites. Other examples of spectra from Ganymede and Callisto will be shown later. Table 5 also summarizes the main features of all of the radar echoes obtained up to 1982 (Ostro, 1982). For comparison, numbers are also given for Earth's Moon which is typical of those for the terrestrial planets; Moon has been studied the most using radar. The first thing that is obviously different between the icy Galilean satellites spectra and that of a terrestrial planet is the size of the spectra. The spectra shown in Figure 3 are normalized by the geometric cross-section of the respective radar target. The total area under the spectrum from the icy Galilean satellite is much larger than that of the terrestrial planet as can also be seen from the first row of Table 5. Europa and Ganymede have larger radar cross-sections than would a perfectly conducting sphere of the same radius as these bodies which would have $\hat{\sigma} = 1$. Another striking difference is that in the Europa spectrum, the spectrum marked SC, which is the spectrum observed in the same circular polarization helicity state as was transmitted, is larger than the spectrum marked OC, which is the orthogonal circular polarization helicity state. This is the reverse of the situation that is observed from a terrestrial planet. Although the linear polarization ratio is not larger than unity, it is significantly larger than that observed for terrestrial planets. The final difference that is of significance for the work here is that the spectrum from the terrestrial planet has a strong feature near zero Doppler frequency, the quasi-specular component, and small refelctivity at other Doppler frequencies, the so called diffuse component. The spectra from the icy Galilean satellites don't appear to divide into these two components; they have significant power at all Doppler frequencies and they don't have a strong, sharply peaked feature at zero Doppler frequency. The power law exponent, m, shown in Table 5 for the Galilean satellites indicates a broad power spectrum as in Figure 3. If every point on the surface scattered isotropically over a hemisphere, then the exponent would be 2; this case is referred to as a Lambert scattering law. The exponent for Moon refers only to the quasi-specular component. The exponent for the diffuse component is probably closer to the size of that of the Galilean satellites.

Recent radar investigations of Saturn's satellite Titan (Muhleman *et al.*, 1990) and the polar ice cap of Mars (Muhleman *et al.*, 1991) show similar radar properties to those of the icy Galilean satellites.

2.3 Previous Models and Analysis

In the next chapter I will discuss the analysis I have done of a model first proposed by Eshleman (Eshleman, 1986a; Eshleman, 1986b). In this section I will discuss four other models that have been proposed to explain the unusual backscattering properties as well as the work done by Eshleman prior to the work to be discussed in the next chapter. Figure 4 shows the essential geophysical structure involved in the five models. Three of these (Ostro and Pettengill, 1978; Goldstein and Green, 1980; Hagfors *et al.*, 1985) preceded the radar glory model of Eshleman and this model shares several of the features of the others. One model (Hapke, 1990) appeared after Eshleman's model. It is perhaps the most attractive model in terms of its geophysical plausibility, but there is no way to use the data in hand to discriminate between the different models. Other types of data such as bistatic radar experiments to explore the phase function of the scattering centers are needed to completely understand the mechanisms causing the unusual scattering by these satellites.

Most of the models involve multiple scattering in order to reproduce the observed polarization behavior. However, the radar glory model of Eshleman and the surface crater model of Ostro and Pettengill involve a small degree of randomness in the placement of the scatterers in a basically deterministic and special geometry whereas the models of Goldstein and Green and Hapke involve complete randomness in the location and orientation of scatterers. The model of Hagfors *et al.* is the only one that does not involve multiple scattering and doesn't invoke any randomness in its inital conception. Eshleman (1986), however, showed that this model would predict a null in the scattering in the backscattering direction unless there were some degree of incoherence involved.

Ostro and Pettengill (1978) showed that the observed polarization properties were consistent with a model in which the radio waves are reflected twice by hemispherical craters on the surface. However, since the craters are on the surface, much of the power is transmitted into the ice and this model is not able to account for the huge radar cross-sections without making the unlikely assumption that the surface refractive index is closer to that of silicate rocks ($n = 2.4$) than that of ice ($n = 1.8$). This is especially unlikely since it would require Europa to have its surface refractive index be the closest to that of silicate rocks and it is known that Europa's surface, of the three icy Galilean satellites, contains the highest ice to rock ratio (see Section 2.1). Ostro (1982) concluded that this model was not very plausible because of the high refractive index material required and because it requires craters that are perfectly hemispherical and too smooth on scales of the wavelength.

Goldstein and Green (1980) proposed that the upper few meters of the surfaces of these satellites are full of randomly oriented cracks and fissures that form voids in the ice with planar facet interfaces between the ice and vaccuum. They recognized that when a plane wave is incident on a planar facet at angles greater than the Brewster angle that the incident sense of polarization is largely preserved. They ran Monte Carlo simulations of photons reflecting from a slab of ice containing such voids with the orientation of the normal to the planar interfaces being completely random and found that this model could account for the observed poarization properties of the icy Galilean satellite radar

echoes. In the best-fit conditions, most of the photons were totally internally reflected from the voids. They found that the scattered energy behaved very much as if it had been scattered by an ideal diffusing screen; thus, the direction of the energy is isotropic. Ostro (1982) found that this calculation of Goldstein and Green had a slight error in it that overestimated the ability of the model to invert the usual polarization behavior and that the model could not simultaneously be fixed to fit the polarization behavior and the huge radar cross-sections. Ostro argues that other scattering mechanisms such as scattering by wavelength sized particles could help to increase the radar cross-sections, but that these single scattering events would rapidly destroy the ability of the model to invert the polarization. Nevertheless, he is able to find a match to the data by requiring that the ice refractive index be very small ($n = 1.2$ in the case of Europa). He points out that such low refractive indices imply low mechanical strength and hence make the assumption that voids could be maintained untenable. He salvages the model by proposing that the voids could be replaced by material of slightly different refractive index from that of ice and of similar strength.

Hagfors *et al.* (1985) concluding that the Goldstein and Green model can't account for the huge radar cross-sections propose a model involving refraction by spherically symmetric inhomogeneities in refractive index below the surface of the ice. They assume that the inhomogeneities are large enough that geometrical optics is valid. Since there are no reflections involved and the incident fields are simply turned around toward the radar, the incident polarization is preserved entirely. Also, they find that there is a caustic in the backscattering direction and thus in the geometrical optics approximation the field is infinite. Thus, they conclude, without calculating the actual radar cross-sections implied by their model which can't be calculated using geometrical optics, that if this scattering mechanism operates in conjunction with other mechanisms that the radar properties of the Galilean satellites are explained by it.

Eshleman (1986) computes the wave optical correction to the infinities predicted by geometrical optics in the Hagfors *et al.* model and finds that when polarization is taken into account that the backscattering from perfectly spherical backscattering lenses would be zero. The principal contribution to the backscattered field comes from a ring or halo around the scattering center and is similar to the optical effect called the glory in which such halos are observed around the shadow of an observer when the incident light comes from behind the observer and the shadow is cast on water drops in a cloud. To salvage this model, he was lead to propose that the glory halos broke up into patches or glints due to azimuthal imperfections in the shape of the lense. The fields were coherent within each such glint that were assumed to be larger than a wavelength in size and the fields from different glints added incoherently.

Eshleman (1986) proposes a modification to the model in which the inhomogeneity in refractive index is a step discontinuity at the wall of a buried crater in which the refractive index goes from some value above the wall to a smaller value below. He argues that there are a number of ways in which such structures could occur. One way involves a cratering event followed by a process (either

sublimation or frost deposition) whereby the surface ice becomes less dense and hence its refractive index becomes smaller than the more solid ice below which is then followed by a resurfacing in which the frost layer is overlain by a more dense ice overburden. Another possibility is that the cratering event itself compacts the ice near the surface of the crater walls which results in a layer of higher refractive index material lining the walls or perhaps the rocky material of the impacting object lines the walls of the crater. In any case, the main features of the model are a hemispheroidal geometry that strongly favors backscattering over scattering in any other direction, a decrease in refractive index at the hemispherical boundary that permits multiple total internal reflections thereby reflecting all the incident power at each reflection and also causing a differential phase insertion in two modes (TE and TM) of reflection, and a slight randomization of the shape that breaks up the glory halo into several coherent patches. This can be taken purely as a prescription of the electromagnetic model without being too specific about the mechanical model that goes with it. The key feature distinguishing this model from the Goldstein and Green model and the Hapke model (to be discussed next) is the specialized structure and the relatively low order of randomness involved in the Eshleman model. The result is that the Eshleman model easily accounts for the polarization inversion and the large cross-sections observed.

Eshleman's analysis does not account for the effects introduced by the interface between the overburden and the vacuum above and he doesn't calculate the shape of the Doppler spectra from this model. The work reported in Chapter 3 completes the analysis of the radar glory model. In that chapter we also consider a possible explanation for the slight frequency dependence indicated in Table 5.

Hapke (1990) and Hapke and Blewett (1991) propose a different model which is like the Goldstein and Green model in that it involves mutiple scattering below the ice surface, but it does not involve total internal refelctions from the scatterers. Hapke proposes that the scatterers are silicate rocks of about wavelength size suspended in the ice. He points out that despite the randomness involved there is a coherence involved in the backscattering direction because for any photon which can find its way through the multiple scatterings back to the radar there is another one that was transmitted from the radar that found its way along the same path but in the reverse direction. Thus those two photons will add coherently. The result is that there is an enhancement in a small range of angles about the backscattering direction where the scattered intensity rises from a diffuse background level to values as much as two times this level in the backscattering direction. He calls this effect the coherent backscattering opposition effect (CBOE). This doubling of the power would also occur in the Goldstein and Green model as well as the Eshleman model. It doesn't appear to have been included in the Goldstein and Green model, but it has been included in the Eshleman model although he didn't point it out explicitly presumably because only backscattering results were being discussed and the only significance of the factor of two for this one direction is that the solution of the problem is incorrect without it. (See section Chapter 3 where the factor of two is explicitly pointed out and

the resulting formulas can be easily seen to agree with Eshleman's.) Hapke does a scalar radiative transfer analysis and hence his calculation of polarization properties is done in an *ad hoc* manner. Nevertheless, Hapke concludes that his model predicts the observed polarization properties, the huge cross-sections, and the broad Doppler spectra. However, to obtain a fit to the large cross-sections he requires scatterers with albedos approaching untiy, that is, with low loss. Peters (1992) did a more rigorous perturbation calculation including polarization effects for the Hapke physical model and found that if the scatterers are anisotropic, that is, they are forward scatterers implying they are of wavelength or larger size, then the polarization ratios computed from his analysis are consistent with those observed. In his paper he only does the comparisons with the polarization ratios and doesn't discuss conditions necessary to fit the cross-sections.

Chapter 3

Analysis of Radar Glory Backscattering

3.1 General Considerations for Scattering by Satellites

We consider plane waves incident on a spherical planet as shown in Figure 2. We define a satellite-centered cartesian coordinate system with unit basis vectors (e_X, e_Y, e_Z) having e_Z pointing toward Earth and e_X , e_Z , coplanar with the spin axis, Ω, of the planet. We will consider a scattering center located at the point (X, Y, Z). It will be convenient to also define angular coordinates (Θ, Φ) of the scattering center as shown in Figure 2.

The incident field is a time harmonic travelling wave with frequency ω_0, wavelength λ_0, and wavenumber $k_0 = 2\pi/\lambda_0$. The medium is vacuum with permeability μ_0, and permittivity ε_0 so that the wave phase velocity is $c = \sqrt{\mu_0 \varepsilon_0}$, and the wave impedance is $\eta_0 = \sqrt{\mu_0/\varepsilon_0}$. In the planet-centered coordinate system the incident field is,

$$\boldsymbol{E}^i = \left(E^i_X \boldsymbol{e}_X + E^i_Y \boldsymbol{e}_Y\right) e^{(-ikZ - i\omega_0 t)} \tag{1}$$

$$\boldsymbol{H}^i = -\frac{1}{\eta_0} \boldsymbol{e}_Z \times \boldsymbol{E}^i \tag{2}$$

where E^i_X and E^i_Y are constant, complex amplitudes. We will consider both linearly polarized and right-hand circularly polarized incident fields. The linear polarized case will have its electric field vector at an angle Φ_P with respect to the X-axis. For the linearly polarized case,

$$E^i_X = E^i \cos \Phi_P \tag{3}$$

$$E^i_Y = E^i \sin \Phi_P \,. \tag{4}$$

For the circularly polarized case,

$$E^i_X = E^i \tag{5}$$

$$E_Y^i = -iE^i \tag{6}$$

We are interested in calculating the radar cross-section for backscattering of two orthogonal components of the electromagnetic field, either the same linear (SL) and orthogonal linear (OL) or the same circular (SC) and orthogonal circular (OC) relative to the transmitted polarization. The reflected field, E_P, where P indicates the polarization, is time varying with a deterministic component that is a rapidly oscillating signal modulated by the Doppler shifted and time delayed contributions from the many scattering centers and a random component due to the many scattering events that contribute to the backscattering from a particular scattering center which is usually treated in a statistical manner. (Actually, there is no randomness involved because there is only one realization of the scatterers and there is no relative motion, random or otherwise, between the scatterers. Thus, the detailed time variation of this 'random' component of the reflected signal contains information about the scattering process, but it is too much information relating to the properties and locations of each individual scatterer. There is no way to use all this information. In order to reduce the amount of information we forgo any detailed knowledge of the properties and locations of the individual scatterers and opt for a statistical treatment of those properties in which we only describe the mean and perhaps standard deviation of those properties and hence of the time varying reflected signal.) Define $E_P(X,Y)$ to be the backscattered field received at Earth due to a scattering center of area dA located at the point $(X, Y, \sqrt{R^2 - X^2 - Y^2})$ on the surface of the satellite (refer to Figure 2). This field is time varying consisting of a time harmonic component at the Doppler shifted frequency ω given by

$$\omega - \omega_0 = 2k_0 Y \Omega \sin \Psi \tag{7}$$

and a random component due to the many backscattering events included in the area dA (neglecting other time variations that are removed as discussed in Section 2.2). The radar cross-section of this scattering center is then defined as (Green, 1968),

$$\sigma_P(X,Y) = 4\pi r_E^2 \frac{\overline{|E_P(X,Y)|^2}}{|E^i|^2} \tag{8}$$

where the line over $|E_P(X,Y)|^2$ indicates an infinite time average. I will write this as

$$\sigma_P(X,Y) = N\langle\sigma_P(X,Y)\rangle \tag{9}$$

where $\langle\sigma_P(X,Y)\rangle$ indicates the expected value (*i. e.*, ensemble average) of the radar cross-section for a single backscattering event and N is the number of backscattering events within the area dA. We also define the specific cross-section (the cross-section per unit area of surface also known as the surface scattering coefficient (Ulaby *et al.*, 1981)),

$$\sigma_P^\circ(X,Y) \equiv \frac{d\sigma_P}{dA} = \rho(X,Y)\langle\sigma_P(X,Y)\rangle \tag{10}$$

where σ_P is the total cross-section from all scattering centers and $\rho(X,Y)$ is the number density of backscattering events on the surface.

The total reflected field E_P is again time varying due to the time delays and Doppler shifts from the individual scattering centers. Since the icy Galilean satellites are overspread and CW signals are used, we assume that the sampling rate of the signal is larger than any of the time delays due to the radar depth of the target. The magnitude squared of the Fourier transform of E_P in a frequency band $(f, f+df)$ is proportional to the total radar cross-section σ_P due to many scattering centers located in a strip of width dY parallel to the X-axis centered at Y corresponding to f. The specific radar cross-section from this strip is,

$$\sigma_P^o(Y) \equiv \frac{d\sigma_P}{dY} = \int_{-\sqrt{R^2-Y^2}}^{\sqrt{R^2-Y^2}} \sigma_P^o(X,Y) \sec\Theta \, dX \tag{11}$$

where the $\sec\Theta = R/\sqrt{R^2-X^2-Y^2}$ factor is due to the fact that an area $dA = R^2 \sin\Theta \, d\Theta \, d\Phi$ located at polar angle Θ on the spherical surface projects to an area $\sec\Theta \, dX \, dY$ on the XY-plane. The total radar cross-section of the target is then given by one more integration,

$$\sigma_P = \int_{-R}^{R} \sigma_P^o(Y) \, dY \tag{12}$$

Once we calculate the average cross-section of a single backscattering event, that is, $\langle \sigma_P(X,Y) \rangle$, then we can calculate the specific and total cross-sections, polarization ratios, and Doppler power spectra to compare with the data. In the next section we calculate this for the radar glory model.

3.2 Backscattering from Buried Craters

Figure 5 shows a buried crater from which we wish to calculate the radar cross-section. To analyze the backscattering we use geometrical optics to trace the rays through the ice overburden, through multiple bounces in the crater, and back through the ice-overburden. In the geometrical optics approximation the effects on the amplitude and field divide into purely geometrical considerations relating to the electrical path length of the rays and the spreading of a bundle of rays into a curved wavefront due to the curvature of the boundaries encountered and purely plane wave refraction and reflection effects at the boundaries (the usual assumption is that the radii of curvature of boundaries are large compared to the radius of curvature of the wavefront). Figure 5 shows the multiple effects on the complex amplitude of the electric field. First, the incident Electric field $\boldsymbol{E}^i$ is multiplied by a rotation matrix $\boldsymbol{J}$ to put its components into TE and TM orientations. Then this field is multiplied by the Fresnel transmission coefficients for TE and TM incidence which is accomplished by multiplying by the matrix $\boldsymbol{T}_{in}$. Then we multiply by a rotation matrix $\boldsymbol{K}$ to put this transmitted field's components into TE and TM orientations for reflection from the walls of the crater. It turns out that for a spherical geometry such as we are assuming for the crater walls, the multiple

bounces lie in a plane, so the TE and TM components do not change orientation at each bounce. Then at each bounce we multiply by the Fresnel reflection coefficients appropriate for TE and TM incidence contained in the matrix $\boldsymbol{R}$. These coefficients can be complex valued. Then we multiply by a geometrical divergence factor D accounting for the fact that after reflection from the curved boundary, *i.e.*, the crater walls, the wave front's curvature is altered. Since the geometry at each bounce is the same, after N bounces through the crater we multiply by N reflection matrices $\boldsymbol{R}^N$ and the divergence factor D_N (it is not simply a product of N divergence factors). Then, we multiply by a rotation matrix $\boldsymbol{K}^{-1}$ to put the electric field components into TE and TM orientations appropriate for refraction back out of the ice which then contributes the factor $\boldsymbol{T}_{out}$. Then we multiply by the divergence factor D_{out} appropriate for transmission of a curved wavefront through a planar interface. Finally, we multiply by the rotation matrix $\boldsymbol{J}^{-1}$ to put the electric field components back into the orientations of the incident field.

It turns out that there are a few other effects that must be considered. Figure 5 only shows one possible ray that makes it back to Earth. There are an infinite number of rays possible that make it back to Earth. If we look below the surface of the ice at the intersection of all these rays with a plane orthogonal to their path, we find they all lie on a circle of radius $r_o \sin\theta$ where r_o is the radius of the crater and θ is the angle between the incident ray and the normal of the crater at each bounce in the crater. If we look in the plane orthogonal to the Earthward bound rays above the ice (shown in Figure 5), this circle becomes an ellipse in general. So, to compute the total field at Earth we have to add up the contribution from all these rays. The result is infinite; there is a caustic in the geometrical optics field in the backscattering direction. A number of methods are available to correct for this result without totally abandoning the geometrical optics approach. One method is to use the geometrical optics field on the plane indicated in Figure 5 and the Kirchoff diffraction integrals in the Fraunhoffer approximation to propagate the fields to Earth. Another method is Maslov's method (Maslov and Fedoriuk, 1981; Ziolkowski and Deschamps, 1984; Kravtsov, 1968) which constructs the geometrical optics field in 6 dimensional phase space (3 spatial and 3 wavevector components) where there is no caustics anywhere and then uses a hybrid 3 dimensional space consisting of some spatial and wavevector dimensions to compute the field on the caustic. Either method gives the same result which is finite.

Another effect is that at some value of Θ the crater rim will obstruct some of the rays and prevent them from returning to Earth. The result is that the glory circles below the ice, ellipses above the ice will not be complete; they will break up into two arcs. Another effect is that we don't expect that these craters are perfectly shaped and it is proposed that these glory arcs break up into patches or glints (Figure 6). The fields from each glint are assumed to be coherent, but the fields from two different glints add incoherently. The one exception is the two glints that are at opposite ends of a diameter of the glory circle below the ice. For a ray that travels through the path indicated in Figure 5, there is another ray that travels the exact opposite path. The fields associated with these

two rays add coherently and they come from the two glints mentioned.

The radar cross-sections for fields received in the orthogonal and same linear (OL and SL respectively) polarizations and those for fields received in the orthogonal and same circular (OC and SC respectively) polarizations are

$$\sigma_{SL}(\Theta,\Phi) = CA_L(3 - x_L) \quad , \quad \sigma_{OL}(\Theta,\Phi) = CA_L(1 + x_L) \tag{13}$$

$$\sigma_{SC}(\Theta) = 2CA_C(1 + x_C) \quad , \quad \sigma_{OC}(\Theta) = 2CA_C(1 - x_C). \tag{14}$$

$$C = \frac{\pi r_o^2 FH}{\lambda_0} \tag{15}$$

where F is the fraction of the glory arcs filled by glints, H is defined in Figure 6, and λ_0 is the radar wavelength. The A's and x's are (assuming total internal reflections occur; I'll write the more general expressions later) given by

$$A_L = \frac{1}{2}\hat{\sigma}_0\{[(T_1^2 + T_2^2) + (T_1^2 - T_2^2)\cos 2(\Phi - \Phi_P)][\phi_0 - (1 + x)\delta] + 2T_1T_2(1 + x)\delta\} \tag{16}$$

$$\begin{aligned} A_L X_L = \hat{\sigma}_0\{ \quad & 2T_1T_2x\phi_0 \\ & +[(T_1^2 - T_2^2)\cos 2(\Phi - \Phi_P) - (T_1^2 + T_2^2)\cos 4(\Phi - \Phi_P)][\phi_0 - (1 + x)\delta] \\ & +2T_1T_2[3(1 + x)\delta - x\phi_0]\cos 4(\Phi - \Phi_P)\} \end{aligned} \tag{17}$$

$$A_C = \hat{\sigma}_0\{(T_1^2 + T_2^2)\phi_0 - (T_1 - T_2)^2(1 + x)\delta\} \tag{18}$$

$$A_C X_C = 2\hat{\sigma}_0 T_1 T_2 x\phi_0 \tag{19}$$

where

$$\hat{\sigma}_0 = \frac{\sin 2\theta}{N}\mathcal{D}\,, \tag{20}$$

$n_{01}\sin\Theta' = \sin\Theta$, Φ_P is the direction of polarization for the linear polarization case,

$$T_1 = 4n_{01}\cos\Theta\cos\Theta'/(\cos\Theta + n_{01}\cos\Theta')^2 \tag{21}$$

is the product of the TE Fresnel transmission coefficient for the ray entering the ice and the TE Fresnel transmission coefficient for the ray exiting the ice,

$$T_2 = 4n_{01}\cos\Theta\cos\Theta'/(n_{01}\cos\Theta + \cos\Theta')^2 \tag{22}$$

is the same product for the TM fields,

$$x = \cos[2N\tan^{-1}(\cos\theta(\sin^2\theta - n^2)^{1/2}/\sin^2\theta)] \tag{23}$$

is the mode decoupling factor defined in Eshleman (1986),

$$\delta = \phi_0/4 - \sin(4\phi_0)/16\,, \tag{24}$$

and $\phi_0 = \pi/2$ if no shadowing occurs or $\sin\phi_0 = \cot\theta\cot\Theta'$ when this last definition has a real solution. The factor D accounts for possible defocusing of the wavefront as it emerges from the ice into vacuum. Since Eshleman (1986) doesn't consider the effects of the ice overburden he doesn't include this factor, *i.e.*, he has

$$\mathcal{D} = 1\,. \tag{25}$$

If the ice overburden is very thick, then the wavefront encountering the ice is spherical and

$$\mathcal{D} = \frac{\cos^2\Theta}{n_{01}^2\cos^2\Theta'} \tag{26}$$

. We believe these two formulas for $\mathcal{D}$ provide upper and lower bounds respectively on the cross-sections.

Figure 7 shows the dependence of A and x on the relative refractive index, n, of the layer of lower refractive index below the crater (relative to the refractive index of the ice overburden) and the number of bounces, N, for a crater at $\Theta = 0$. The best fit to the observed total power in the various polarizations is given by $x = 0.23$ and $N = 3$.

Figure 8 shows the variation in the radar cross-sections with respect to colatitude Θ and the shapes of the glory arcs. Surface craters and buried craters are compared. Of course the size of the radar cross-sections for the surface craters are much smaller than those of the buried craters.

If we assume the density of craters is uniform across the surface of the satellite, then we can use eqs. (10), (11), and (12) to compute the Doppler spectra and total cross-sections. The resulting equations would look similar to those given above for a single crater except that now the A's and x's are integrals of the previous expressions across the surface and the constant C becomes,

$$C = \frac{M\pi r_o^2}{4\pi R^2}\frac{FH}{\lambda} \tag{27}$$

where M is the total number of buried craters on the surface of the satellite. Thus, C is proportional to the density of buried craters on the surface and is a free parameter to be determined by fitting to the observations.

(Eshleman, 1986b) noted that a wavelength dependence that has been observed in the relative amounts of power reflected in the orthogonal polarizations could be due entirely to a wavelength dependence in the parameter x. One way that x may be wavelength dependent is if the refractive index at the crater walls makes a smooth transition from n_{01} to n_{02}. Here we will model the transition zone as a locally planar layer of thickness d with an exponentially decreasing refractive index (Figure 9) because this is the simplest profile that admits an analytic solution for both TE and TM modes. The solution is in terms of Bessel functions whose order depend on $kl\sin\theta$ where l is the scale height of the exponential and θ is the angle of incidence of the rays at the crater wall.

3.3 Comparison of Theory with Observations

In the previous papers (Eshleman, 1986a; Eshleman, 1986b; Eshleman, 1987), it was found that x=0.23 is required to achieve a close fit to the observations for all three moons. There are several ways to get x=0.23, but the one that seems most likely is the three-bounce case involving TIR. This requires the hypothesis that n=0.7967. The first three rows of Table 6 compare the observed total radar cross-section and the ratios of the orthogonal components of the circular and linear polarization cross-sections with the predictions of the model. For $\hat{\sigma}$ under the theory column we have used C=1 and given the upper and lower bounds based on the new analysis and the analysis in Eshleman (1986) respectively. In order to match $\hat{\sigma}$ for Europa we require C=3.9 or 0.7 depending on the importance of a defocusing effect that was included in the above formulas. If FH/λ were 10 (say F=.5, H=2m, and λ=.1m), then the buried crater model requires 39% or 7% coverage of the moon's surface by glory craters. Also, note the excellent fit between the polarization ratios for Europa and Ganymede at 12.6cm.

The last two rows of Table 6 characterize the shape of the power spectra in terms of an exponent for a $\cos^m \Theta$ fit to the actual curves. The power in narrow frequency bands is an integration over many craters on lines which are orthogonal to the line of sight and parallel to the spin axis of the moon. The theoretical numbers are based on the new analysis that we have called the lower bound. We don't know yet to what degree the depth of the glints below the surface will affect the shape of the spectra. A comparison between the m values provide new support for the buried crater model. However, they do indicate that the theoretical spectra are narrower than the observed spectra. Also, the m_{OC}/m_{SC} values indicate that the observed OC spectra are a little narrower than the SC spectra while the model has the opposite trend.

It is not clear how precisely a theory needs to match these exponents since the observed power spectra are full of additional structure that is not modelled well by the assumed law. The plots in Figure 10 show typical spectra for Europa, the $\cos^m \Theta$ fit to the data, and the spectra computed for the buried crater model. This clearly shows that a precise fit to m is not necessary to produce simulated spectra that model the data quite well. We also show for comparison simulated spectra for Earth's moon based on empirical formulas determined by Evans (1957), where the SC echo is so weak that it is not visible at the scale shown.

In Table 5 we see that Ganymede has been studied at two wavelengths and that there is a wavelength dependence in these observations. Here, we have only addressed the dependence indicated for $\hat{\sigma}_{SC}/\hat{\sigma}_{OC}$. To explain the μ_C data for Ganymede, x must go from about 0.22 at λ=12.6 cm to about 0.33 at λ=3.5 cm. Based on the assumption of a gradient in the refractive index at the crater walls as described in the last section, we have computed, in Figure 11, x as a function of d/λ for a single crater at $\Theta = 0$. We have found that the x value of a single crater is very nearly the same as the x value for the entire moon. The 12.6 cm point is determined where x=0.22 and then the 3.5 cm point is determined by the ratio of wavelengths. The x value is seen to increase with decreasing

wavelength which is consistent with the data. If this is indeed the cause of the dependence, radar measurements at different λ would be extremely sensitive to the specific subsurface conditions on these moons.

Chapter 4

Conclusion

The radar glory model is able to account for all the main features in the radar backscattering data from the icy Galilean satellites. In the previous chapter we presented the geophysical model in terms of a special structure involving buried hemispherical craters in which the refractive index abruptly decreases at the crater wall. It is not known if such a structure actually exists or how it could be formed in detail. It may even be possible that the structure is not formed from a cratering event and that the required variation in refractive index is due to changes in the ice crystalline state as discussed in Section 2.1. We were led to this model via the electromagnetic requirements for producing the observed echoes. It does not seem possible to produce the large radar cross-sections with a model such as that of Hapke (1990) or of Goldstein and Green (1980) involving complete randomness in the scattering mechanism. It seems that something more than the factor of two enhancement due to the coherent backscattering opposition effect discussed by Hapke is needed and that is what leads us to believe that a low degree of randomness imposed on a basically deterministic geometry that favors backscattering is required. In addition to this, though, total internal reflection also needs to occur to produce the large cross-sections and this conclusion is common to both the radar glory model and the Goldstein and Green model. Thus we conclude that these main features of the electromagnetic model—the low degree of randomness imposed on a deterministic geometry that favors backscattering such as a hemisphere and total internal reflection—are important ingredients of the true explanation and provide some information regarding the geophysical structures required. Unfortunately, the data do not sufficiently constrain the models and additional data types are needed to discriminate between the competing theories.

Bibliography

Burns, J. A. (1986). Some background about satellites. In Burns, J. A. and Matthews, M. S., editors, *Satellites*, pages 1–38. The University of Arizona Press, Tucson.

Campbell, D. B., Chandler, J. F., Pettengill, G. H., and Shapiro, I. I. (1977). Galilean satellites of Jupiter: 12.6-centimeter radar observations. *Science* **196**, 650–653.

Eshleman, V. R. (1986a). Mode decoupling during retrorefraction as an explanation for bizarre radar echoes from icy moons. *Nature* **319**, 755–757.

Eshleman, V. R. (1986b). Radar glory from buried craters on icy moons. *Science* **234**, 587–590.

Eshleman, V. R. (1987). The radar-glory theory for icy moons with implications for radar mapping. *Advances in Space Research* **7**, (5)133–(5)136.

Evans, J. V. (1957). The scattering of radio waves by the moon. *Proceeding of the Physical Society B* **70**, 1105–1112.

Evans, J. V. and Hagfors, T., editors (1968). *Radar Astronomy*. McGraw-Hill, New York.

Gaffney, E. S. and Matson, D. L. (1980). Water ice polymorphs and their significance on planetary surfaces. *Icarus* **44**, 511–519.

Goldstein, R. M. and Green, R. R. (1980). Ganymede: Radar surface characteristics. *Science* **207**, 179–180.

Goldstein, R. M. and Morris, G. A. (1975). Ganymede: Observations by radar. *Science* **188**, 1211–1212.

Green, Jr., P. E. (1968). Radar measurements of target scattering properties. In (Evans and Hagfors, 1968), pages 1–75.

Hagfors, T. and Evans, J. V. (1968). Radar studies of the moon. In (Evans and Hagfors, 1968), pages 219–270.

Hagfors, T., Gold, T., and Ierkic, H. M. (1985). Refraction scattering as origin of the anomalous radar returns of Juptier's satellites. *Nature* **315**, 637–640.

Hapke, B. (1990). Coherent backscatter and the radar characteristics of outer planet satellites. *Icarus* **88**, 407–417.

Hapke, B. and Blewett, D. (1991). Coherent backscatter model for the unusual radar reflectivity of icy satellites. *Nature* **352**, 46–47.

Hobbs, P. V. (1974). *Ice Physics.* Clarendon Press, Oxford.

Hudson, R. S. and Ostro, S. J. (1990). Doppler radar imaging of spherical planetary surfaces. *Journal of Geophysical Research* **95**(B7), 10,947–10963.

Kravtsov, Y. A. (1968). Two new asymptotic methods in the theory of wave propagation in inhomogeneous media (review). *Soviet Physics—Acoustics* **14**, 1–17.

Maslov, V. P. and Fedoriuk, M. V. (1981). *Semi-Classical Approximation in Quantum Mechanics.* D. Reidel.

Muhleman, D. O., Butler, B. J., Grossman, A. W., and Slade, M. A. (1991). Radar images of Mars. *Science* **253**, 1508–1513.

Muhleman, D. O., Goldstein, R., and Carpenter, R. (1965a). A review of radar astronomy—part I. *IEEE Spectrum* , 44–55.

Muhleman, D. O., Goldstein, R., and Carpenter, R. (1965b). A review of radar astronomy—part II. *IEEE Spectrum* , 78–89.

Muhleman, D. O., Grossman, A. W., Butler, B. J., and Slade, M. A. (1990). Radar reflectivity of Titan. *Science* **248**, 975–980.

Ostro, S. J. (1982). Radar properties of Europa, Ganymede, and Callisto. In Morrison, D., editor, *Satellites of Jupiter*, pages 213–236. The University of Arizona Press, Tucson.

Ostro, S. J. (1987). Planetary radar astronomy. In *Encyclopedia of Physical Science and Technology*, volume 10, pages 611–634. Academic Press.

Ostro, S. J., Campbell, D. B., Simpson, R. A., Hudson, R. S., Chandler, J. F., Rosema, K. D., Shapiro, I. I., Standish, E. M., Winkler, R., Yeomans, D. K., Velez, R., and Goldstein, R. M. (1992). Europa, Ganymede, and Callisto: New radar results from Arecibo and Goldstone. *Journal of Geophysical Research* **97**(E11), 18227–18244.

Ostro, S. J. and Pettengill, G. H. (1978). Icy craters on the Galilean satellites? *Icarus* **34**, 268–279.

Peters, K. J. (1992). Coherent-backscatter effect: A vector formulation accounting for polarization and absorption effects and small or large scatterers. *Physical Review B* **46**, 801–812.

Smoluchowski, R. (1983). Solar system ice: Amorphous or crystalline? *Science* **222**, 161–163.

Smoluchowski, R. and McWilliam, A. (1984). Structure of ices on satellites. *Icarus* **58**, 282–287.

Thompson, W. R. and Squyres, S. W. (1990). Titan and other icy satellites: Dielectric properties of constituent materials and implications for radar sounding. *Icarus* **86**, 336–354.

Ulaby, F. T., Moore, R. K., and Fung, A. K. (1981). *Microwave Remote Sensing volumes I-III.* Addison-Wesley, Reading, Massachusetts.

Ziolkowski, R. W. and Deschamps, G. A. (1984). Asymptotic evaluation of high-frequency fields near a caustic: An introduction to Maslov's method. *Radio Science* **19**, 1001–1025.

Chapter 5

Tables

Table 1:
Summary of the Physical Characteristics of the Icy Galilean Satellites

Parameter	Europa[a]	Ganymede[a]	Callisto[a]
Orbital Radius[b] (10^3 km)	670.9	1,070	1,883
Radius (km)	1,569	2,631	2,400
Rotational Period (hours)	85.22	171.7	400.5
Density (10^3 kg m^{-3})	2.97	1.94	1.86
Subsolar Surface Temperature[c] (K)	132	155	169
Average Surface Temperature[c] (K)	93	110	120
Geometric Albedo	0.6	0.4	0.2

[a] Unless otherwise stated, data are from Burns (1986).
[b] The orbits of all these satellites are virtually circular.
[c] Data from Gaffney and Matson (1980)

Table 2:
Absorption Length in Ice at Cold Temperatures[a]

$n = 1.8$

	$1/\alpha$ (km)		
T (K)	3.5 cm-λ	12.6 cm-λ	70 cm-λ
90	7.1	66.	1.3×10^3
110	0.94	8.8	1.7×10^2
130	0.23	2.2	43.
150	0.08	0.78	15.

[a] Based on extrapolation formulas given by Thompson and Squyres (1990).

Table 3:
Polymorphs of Ice That May be Present on the Icy Galilean Satellites

Satellite	Polymorphs stable at equator
Europa	II, VI, V, IX
Ganymede	II,I_c
Callisto	I_c

Based on results from Gaffney and Matson (1980)

Table 4:
Bandwidths and Time Dispersions for the Icy Galilean Satellites

		B[a] (Hz)			BT[c]		
Target	T[b] (ms)	3.5 cm-λ	12.6 cm-λ	70 cm-λ	3.5 cm-λ	12.6 cm-λ	70 cm-λ
Europa	10	3670	1020	184	36.7	10.2	1.84
Ganymede	18	3060	850	153	55.1	15.3	2.75
Callisto	16	1190	330	59.4	19.0	5.28	0.95

[a] Bandwidth, $B = 8\pi R/(\lambda_0 P)$ with data from Table 1.
[b] Time Dispersion, $T = 2R/c$ with data from Table 1.
[c] A target for which $BT \geq 1$ is said to be overspread and it is not possible to simultaneously map the surface of the target in Doppler and time delay.

Table 5:
Summary of Radar Data from the Icy Galilean Satellites

	Europa 12.6 cm	Ganymede 12.6 cm	Ganymede 3.5 cm	Callisto 12.6 cm	Earth's Moon 10. cm
$\hat{\sigma}$	$2.60 \pm .64$	1.52 ± 0.4	$1.20 \pm .28$	$0.64 \pm .16$	.05
μ_C	$1.56 \pm .11$	$1.55 \pm .06$	$2.0 \pm .03$	$1.19 \pm .06$	.05
μ_L	$0.47 \pm .07$	$0.47 \pm .08$		$0.55 \pm .10$	$\ll 1.$
m	$1.73 \pm .08$	$1.46 \pm .04$		$1.43 \pm .05$	30.
m_{OC}/m_{SC}	$1.08 \pm .10$	$1.21 \pm .06$		$1.13 \pm .09$	20.

The data for the Galilean satellites are from Ostro (1982). Moon data are from Hagfors and Evans (1968) and Evans (1957): $\hat{\sigma}$ is at 10 cm; the other numbers are at other wavelengths where they were available.

$\hat{\sigma} = (\text{radarcross} - \text{section})/(\pi R^2)$

$\hat{\sigma} = \hat{\sigma}_{SC} + \hat{\sigma}_{OC} = \hat{\sigma}_{SL} + \hat{\sigma}_{OL}$

$\mu_C = \hat{\sigma}_{SC}/\hat{\sigma}_{OC}$

$\mu_L = \hat{\sigma}_{OL}/\hat{\sigma}_{SL}$

m, m_{OC} and m_{SC} are exponents for a least squares fit of the power spectra to a $\cos^m \Theta$ law where Θ is the angle between the radar line of sight and the surface normal of the moon.

Where R is the radius of the particular satellite, C and L refer to circular and linear polarizations, and S and O refer to same and orthogonal to the transmitted polarization.

Table 6:
Comparison Between Observations and Buried Crater Model

	Europa 12.6 cm	Ganymede 12.6 cm	Ganymede 3.5 cm	Callisto 12.6 cm	Buried craters N=3, n=0.7967, C=1
$\hat{\sigma}$	2.60±0.64	1.52±0.40	1.20±0.28	0.64±0.16	0.67 - 3.6
$\hat{\sigma}_{SC}/\hat{\sigma}_{OC}$	1.56±0.11	1.55±0.06	2.0±0.03	1.19±0.06	1.60
$\hat{\sigma}_{OL}/\hat{\sigma}_{SL}$	0.47±0.07	0.47±0.08		0.55±0.10	0.44
m	1.73±0.08	1.46±0.04		1.43±0.05	1.95
m_{OC}/m_{SC}	1.08±0.10	1.21±0.06		1.13±0.09	0.989

The data for the Galilean moons are from Ostro in /7/. $\hat{\sigma} = \hat{\sigma}_{SC} + \hat{\sigma}_{OC} = \hat{\sigma}_{SL} + \hat{\sigma}_{OL}$. m, m_{OC} and m_{SC} are exponents for a least squares fit of the power spectra to a $\cos^m \Theta$ law where Θ is the angle between the radar line of sight and the surface normal of the moon.

Chapter 6

Figures

Figure 1: Arecibo-Galilean satellites geometry. Geometry of radar backscattering from the Icy Galilean satellites.

Figure 2: Satellite Geometry. Convenient coordinates for radar backscattering from a scattering center on a satellite.

Figure 3: Comparison of radar echoes from a terrestrial planet and an icy Galilean satellite.

Figure 4: Five models for backscattering by icy satellites

Figure 5: Buried crater geometry and its effects on radar backscattering

Figure 6: Radar glory arcs and glints

Figure 7: Dependence of A and x on n and N

Figure 8: Variation of buried and surface crater radar cross-section with colatitude

Figure 9: Reflection of electromagnetic field from a layer with an exponentially varying refractive index

Figure 10: Comparison of buried crater Doppler spectra with observations from an icy Galilean satellite

Figure 11: Variation of x for reflection from crater with a layer of material with exponentially varying refractive index

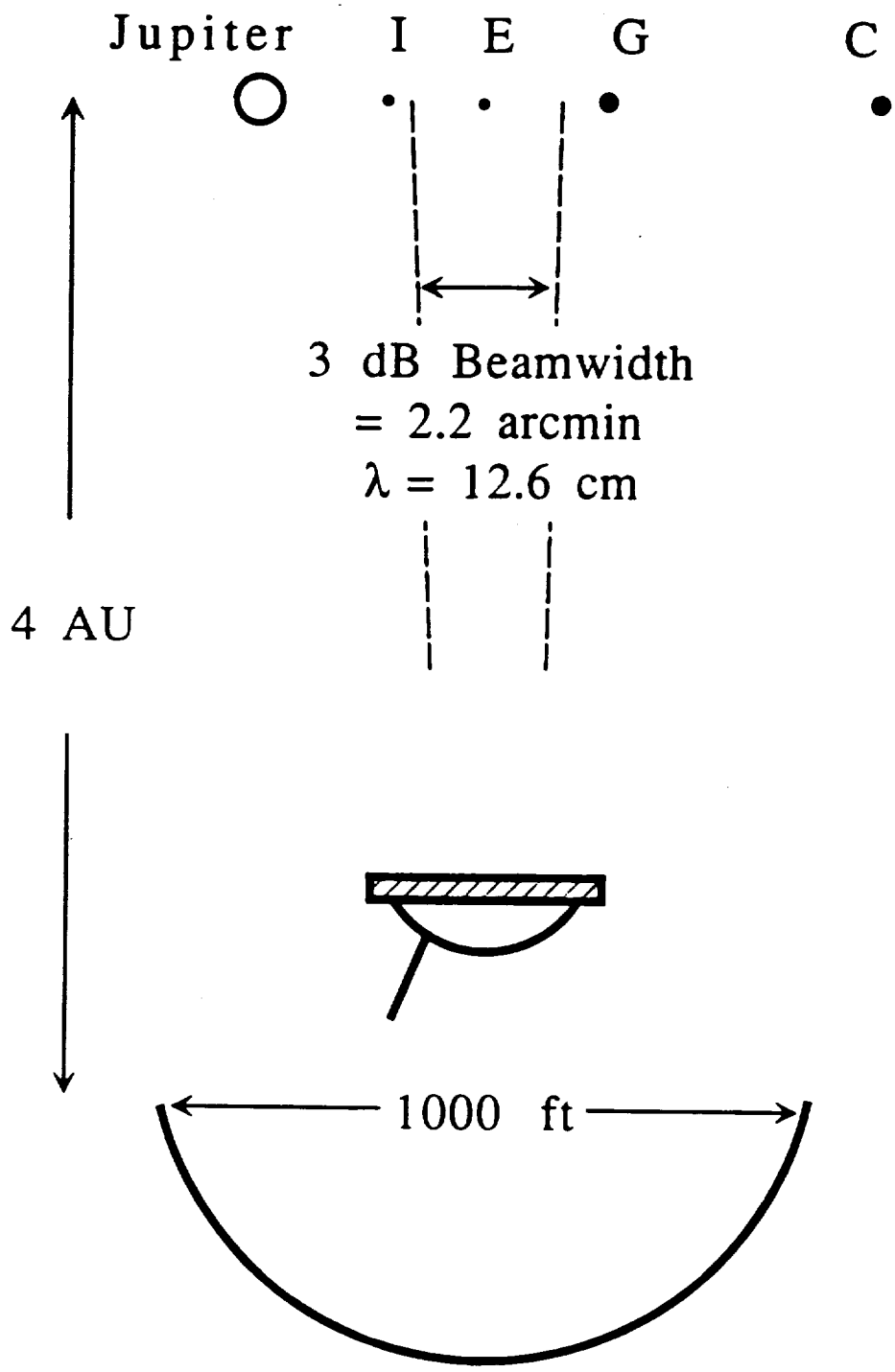
Jupiter
I
E
G
C
3 dB Beamwidth
= 2.2 arcmin
λ = 12.6 cm
4 AU
1000 ft
Arecibo Observatory

Figure 1

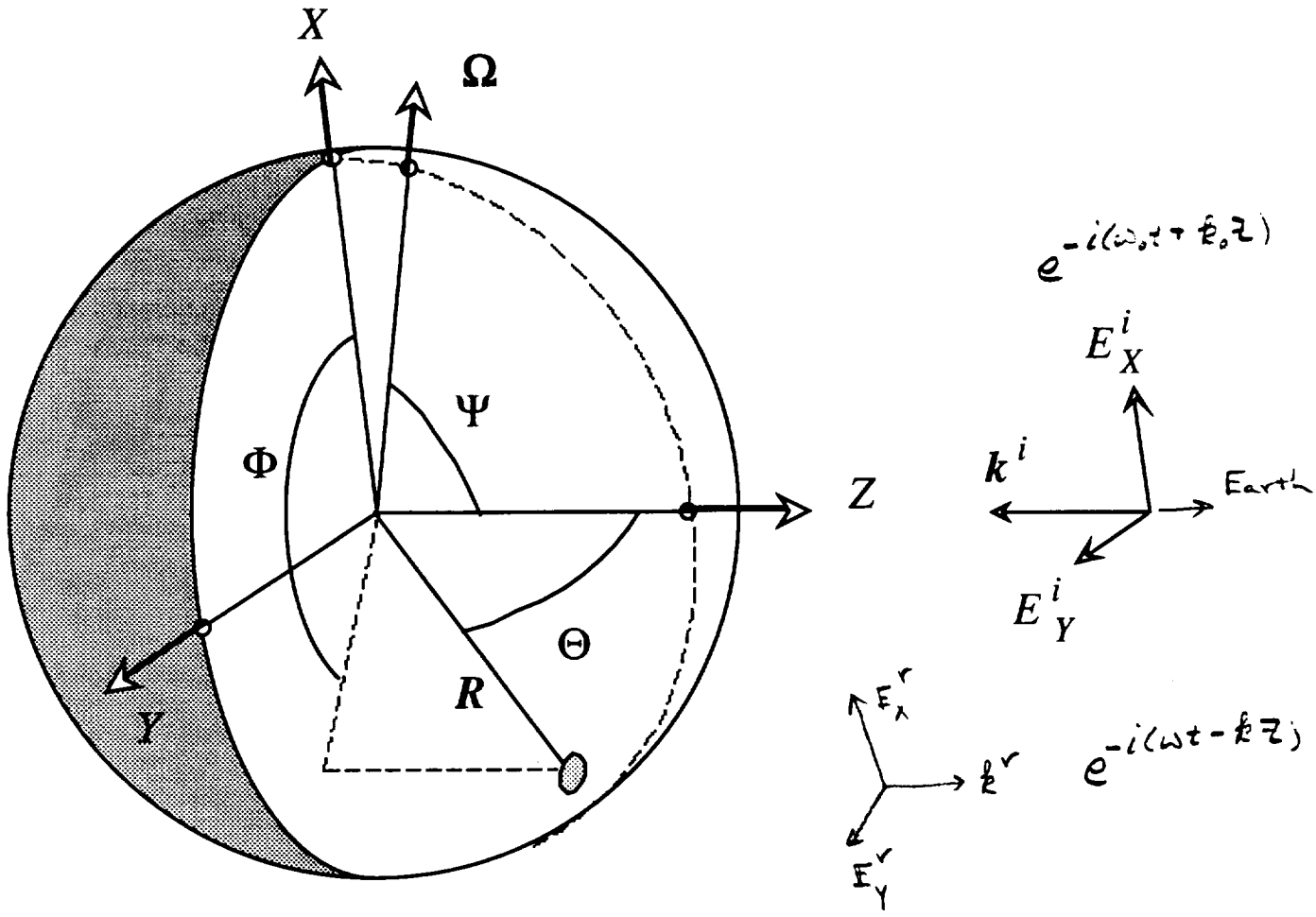
X
Ω
Ψ
Φ
Z
Y
R
Θ
$e^{-i(\omega_0 t + k_0 z)}$
E_X^i
k^i
Earth
E_Y^i
E_X^r
k^r
$e^{-i(\omega t - kz)}$
E_Y^r

Figure 2

From Satellites of Jupiter, D. Morrison ed.
U. of Arizona Press, 1982.

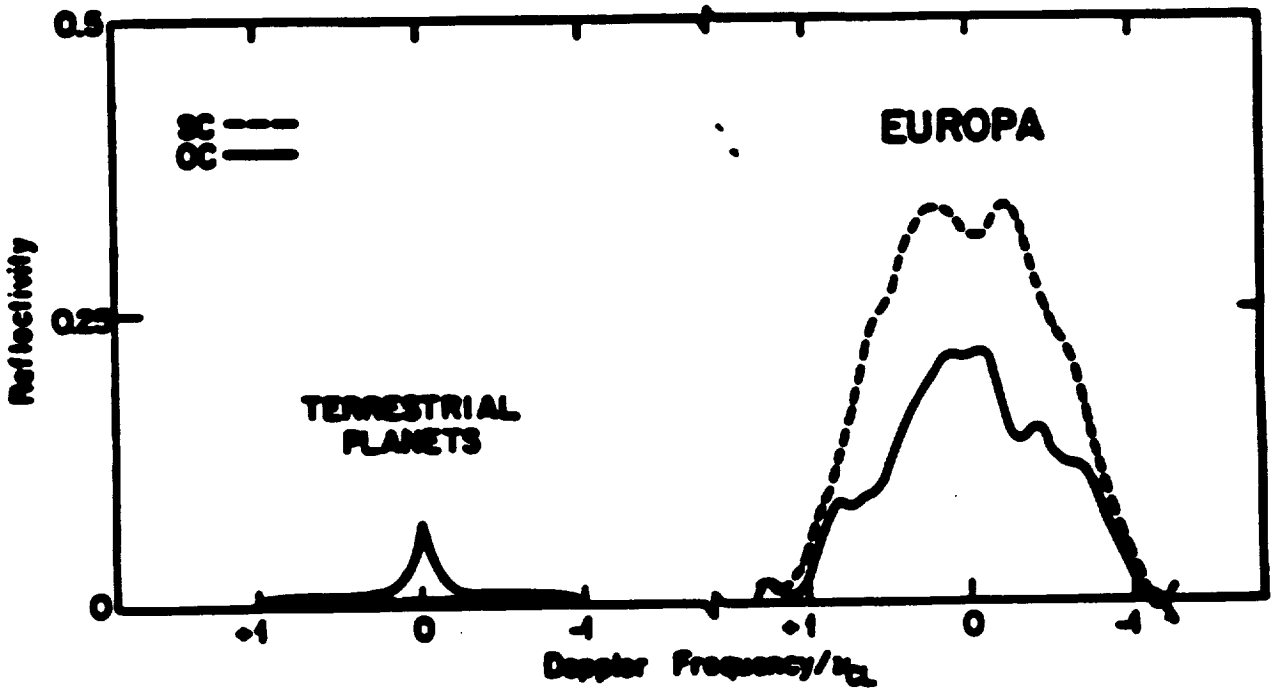

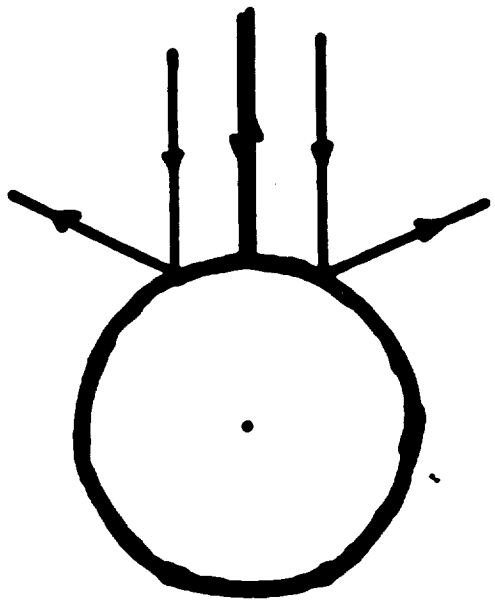

Figure 3

4 Models

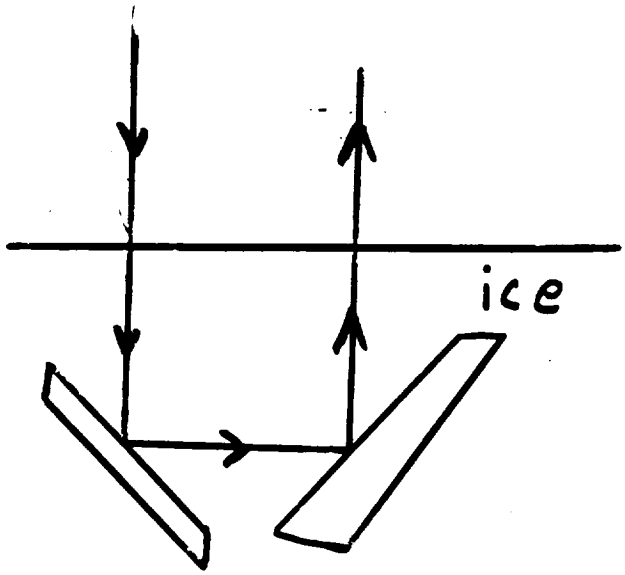

Random Cracks

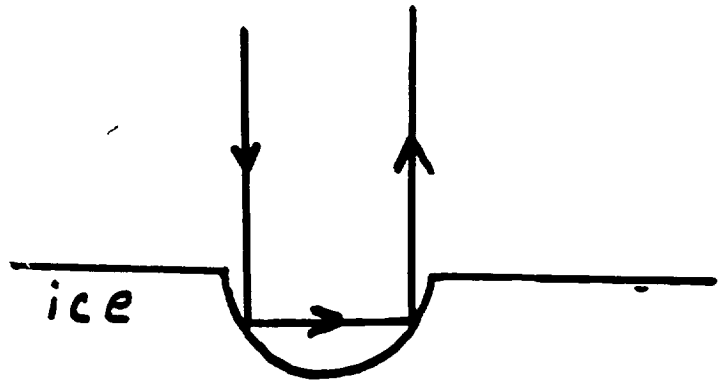

Surface Craters

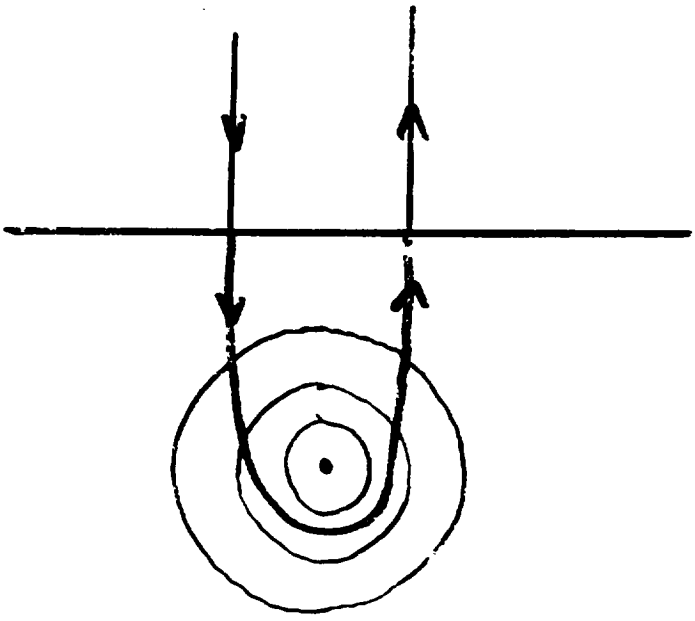

Refraction Centers

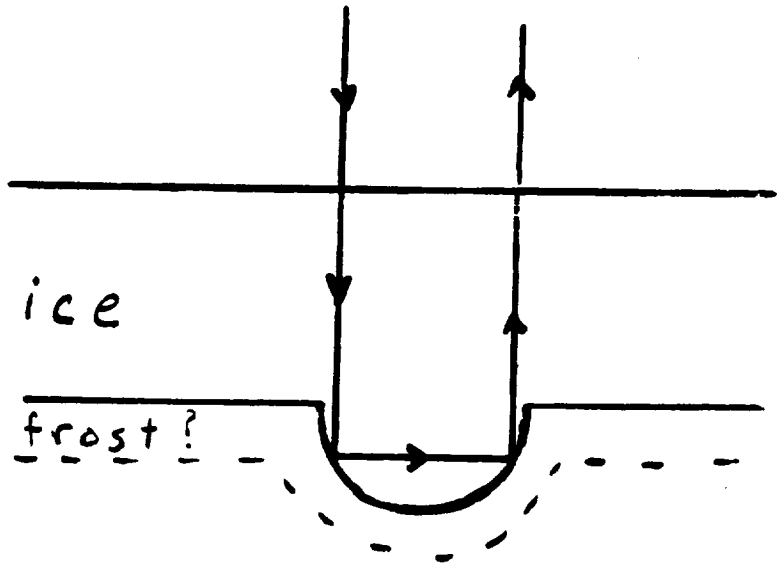

Buried Craters

Figure 4

Figure 5

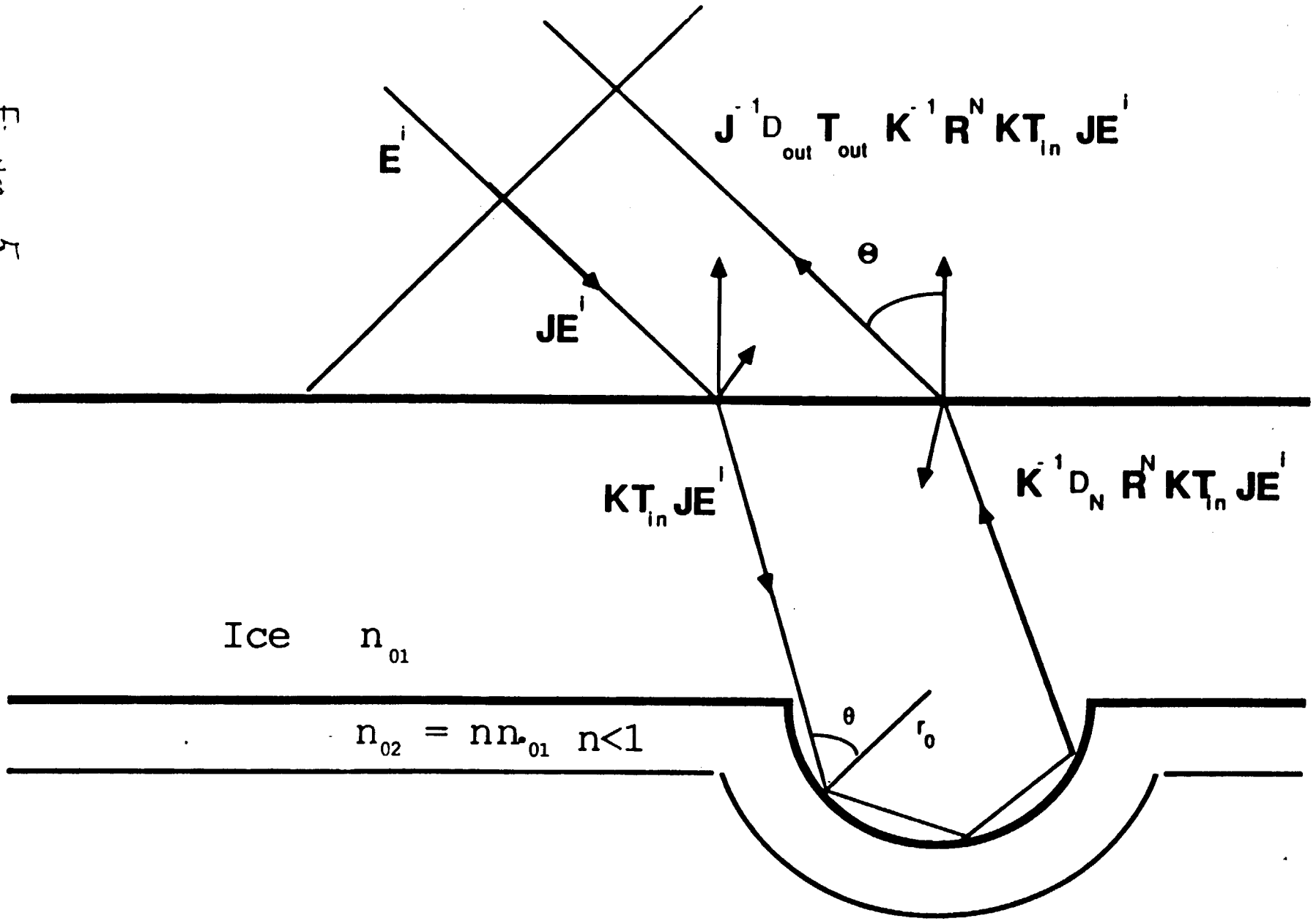

N=3 BURIED CRATER

Glory Arcs

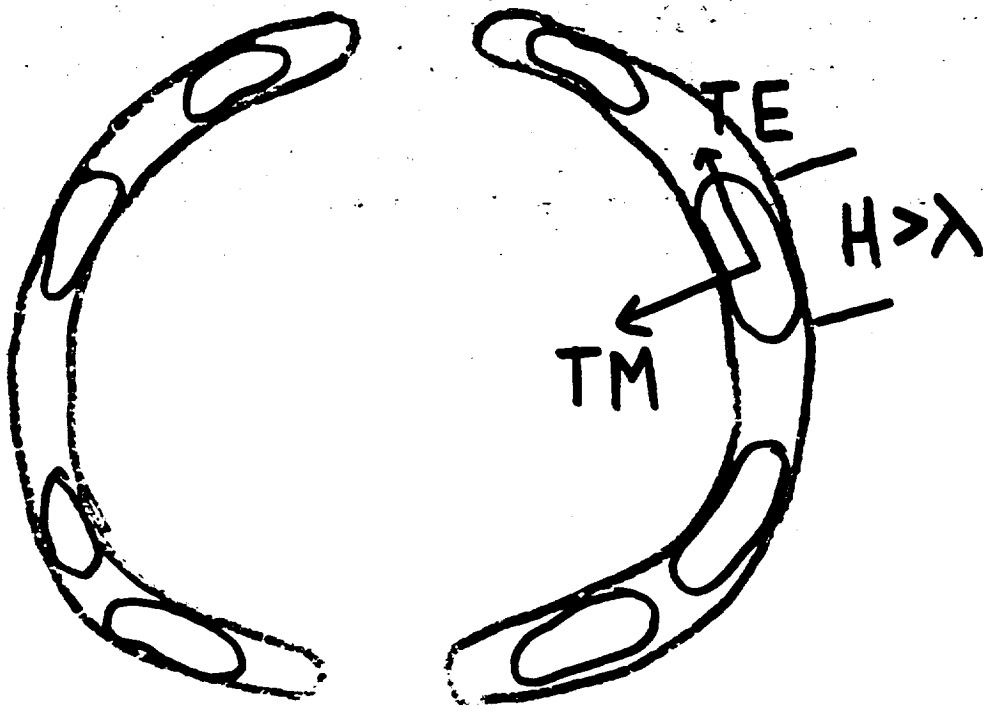

F = fraction of glory arcs filled by glint pairs

Figure 6

$$\hat{\sigma}_{SL} = CA(3-x) \quad , \quad \hat{\sigma}_{OL} = CA(1+x)$$

$$\hat{\sigma}_{SC} = 2CA(1+x) \quad , \quad \hat{\sigma}_{OC} = 2CA(1-x)$$

$$\hat{\sigma} = 4CA$$

$$C = \frac{M\pi r_o^2 FH}{4\pi R^2}\frac{}{\lambda}.$$

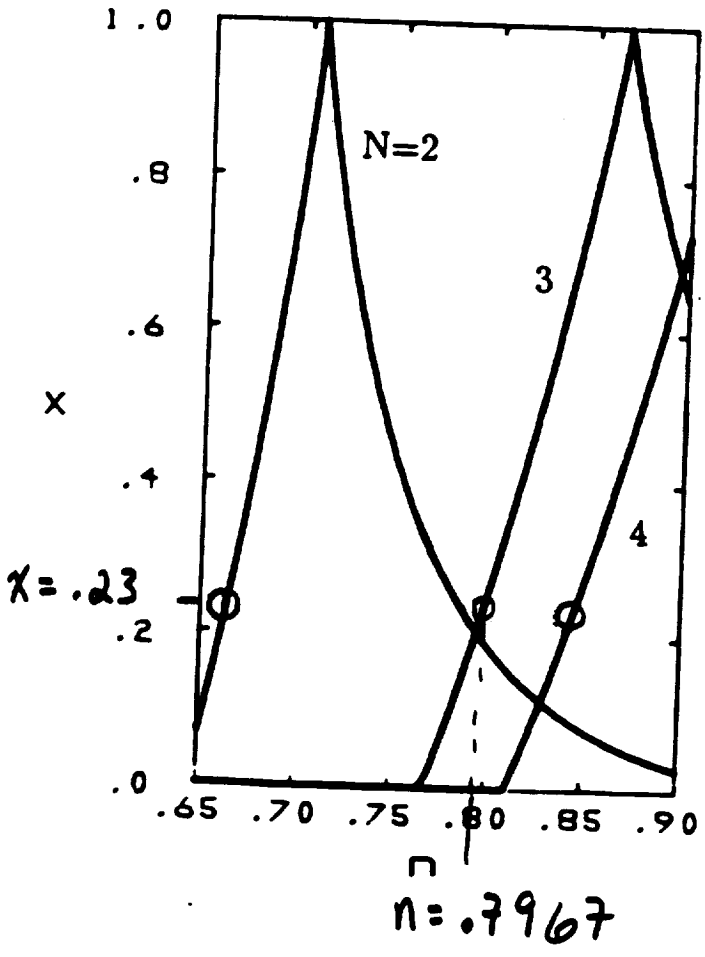

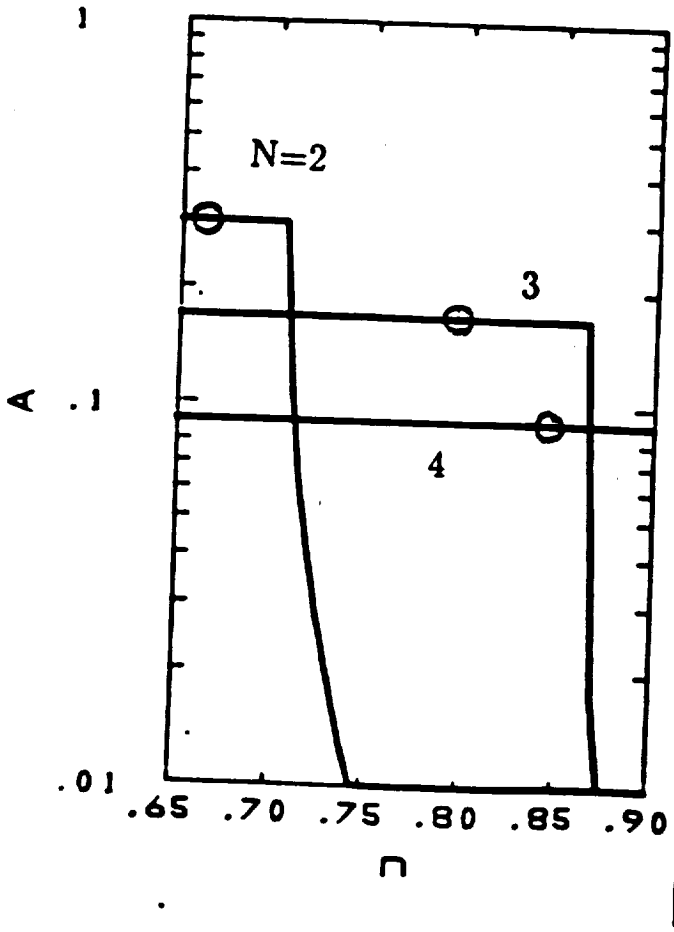

Figure 7

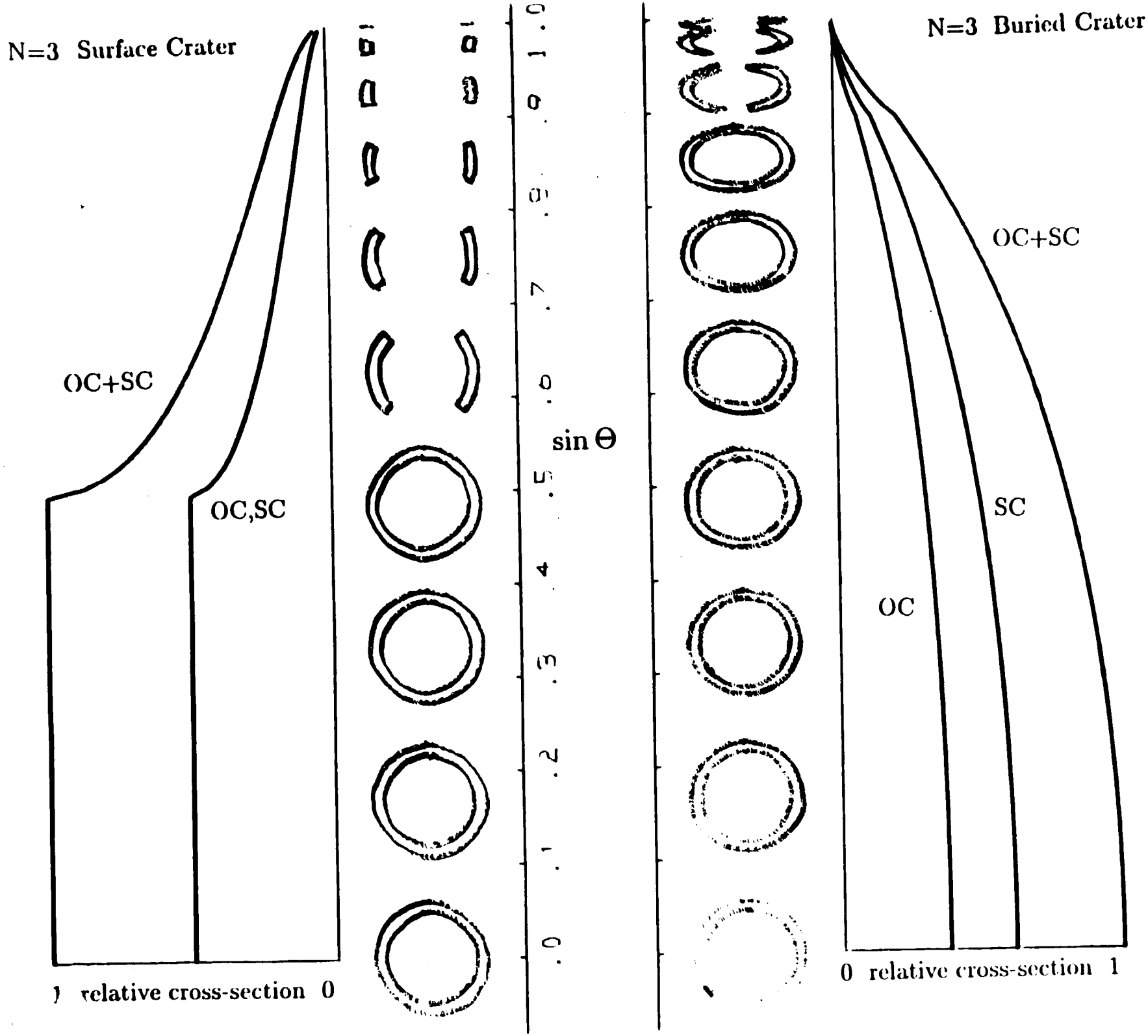
N=3 Surface Crater
OC+SC
OC,SC
1 relative cross-section 0
sin Θ
1.0
.9
.7
.5
.4
.3
.2
.1
.0
N=3 Buried Crater
OC+SC
SC
OC
0 relative cross-section 1

Figure 8

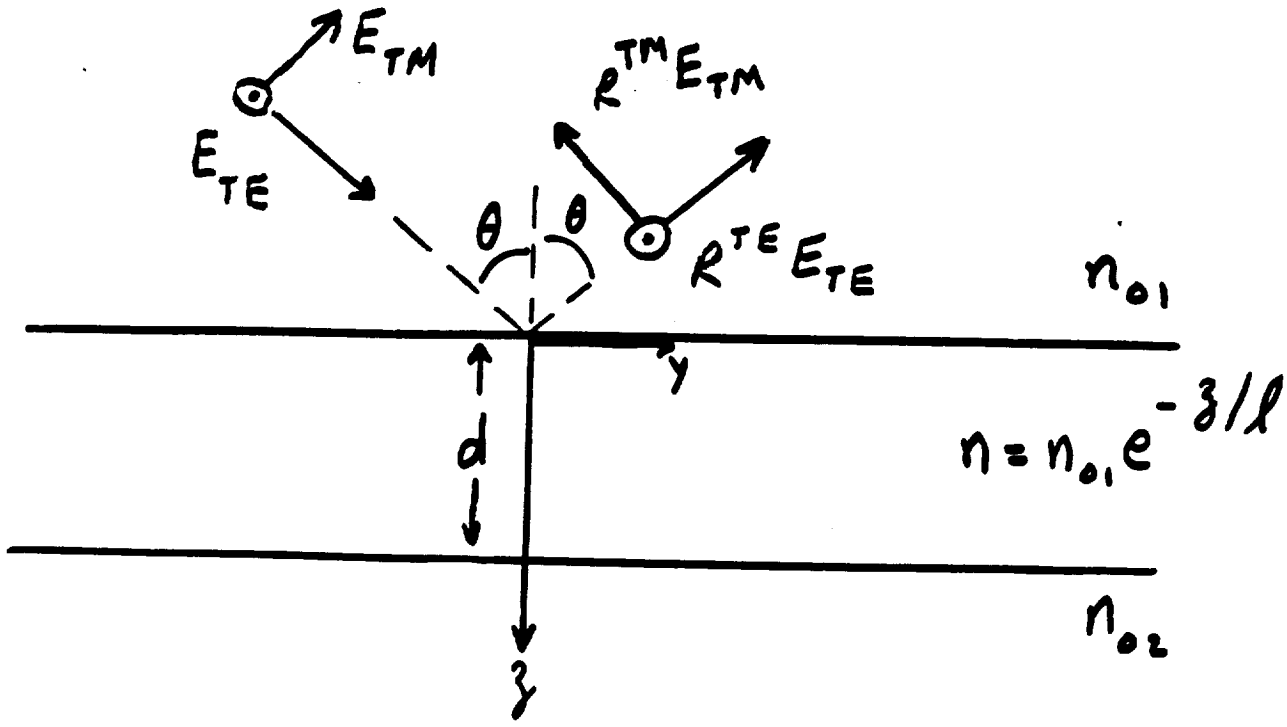

$$l = \frac{d}{\ln(n_{01}/n_{02})}$$

Figure 9

In $z<0$ and $z>d$ the fields are plane waves.

In $0<z<d$:

$$E_{TE} = \left[A J_\nu(kle^{-z/l}) + B Y_\nu(kle^{-z/l})\right] e^{ikysin\theta}$$

$$H_{TM} = \left[C J_\sigma(kle^{-z/l}) + D Y_\sigma(kle^{-z/l})\right] e^{-z/l} e^{ikysin\theta}$$

$$\nu = kl\sin\theta \quad , \quad \sigma = \sqrt{1+\nu^2}$$

Figure 9

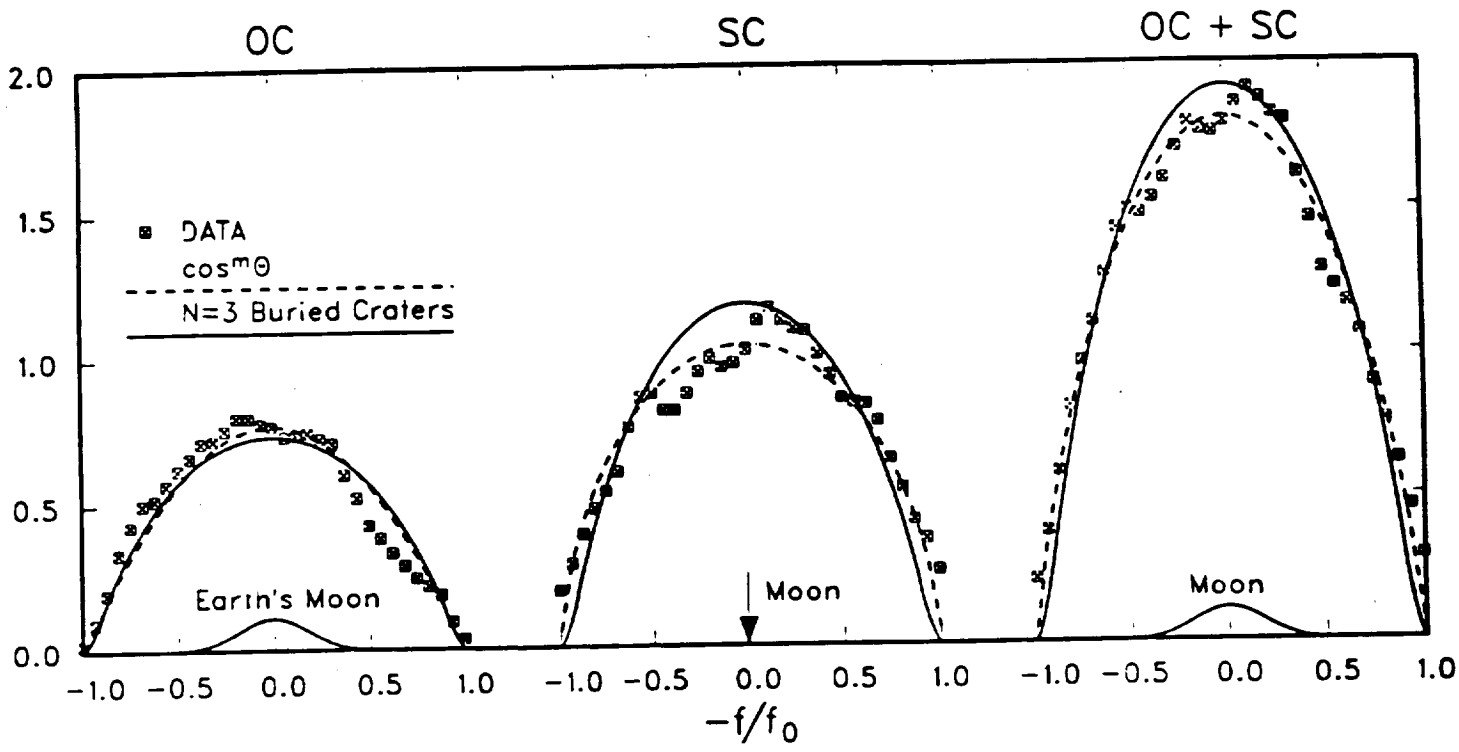

Fig 2. Typical power spectra for circularly polarized waves reflected from Europa compared with the theory and the $\cos^m \Theta$ law. The data are from Ostro /7/ page 221. The exponents for the data(theory) are: m_{oc}=2.14(1.94), m_{sc}=1.22(1.96), and m=1.56(1.95). The data and the theoretical curves have been normalized to σ=2.6; however the $\cos^m \Theta$ curve is not normalized in this manner.

Figure 10

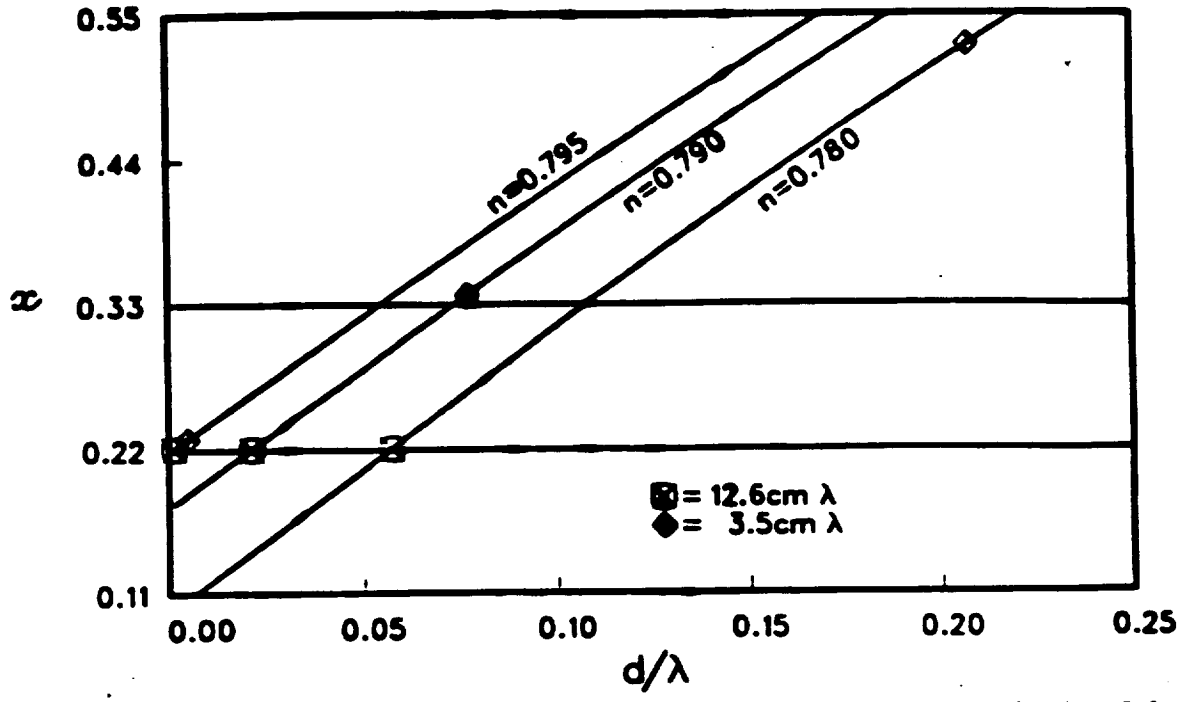

Fig 3. x versus d/λ for three values of n near the optimal value determined for λ=12.6cm.

Figure 11

APPENDIX

Related abstracts and publications

Bull. Amer. Astron. Soc. 20, 873, 1988

Developments in the Buried-Crater Model for Radar Echoes from Icy Moons

E.M. Gurrola, V.R. Eshleman (Stanford University)

The buried-crater model introduced by Eshleman (*Science* 234 587, 1986) has been successful in accounting for anomalously large radar echoes with unexpected polarization ratios that have been observed from three icy moons of Jupiter: Europa, Ganymede, and Callisto. A simple model of a single buried crater with axially incident rays plus a single assumption regarding the ratio of refractive indices in the layers above and below the crater walls was found adequate to model the power in two orthogonal circular and linear polarizations for all three moons.

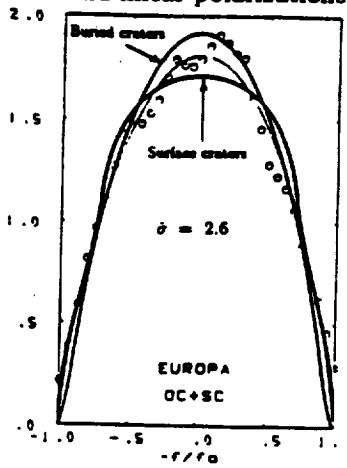

We have found that, with further development of the model to include effects due to angular position of the craters plus a simple assumption of uniform coverage by identical craters, this model also provides a good fit to the only other type of well-established data: the doppler-frequency power spectra. The figure shows theoretical curves of total radar cross-section for buried and surface craters and for a typical Europa spectrum (data from S. Ostro in *Satellites of Jupiter*, D. Morrison, Ed., U. Arizona Press 1982). The light, unlabeled line is a least-squares fit of the data to a $\cos^m \Theta$ law where Θ is the angle between the incident rays and the moon's surface normal. This fit to the data requires 8 times as many surface craters as buried craters. The buried-crater fit gives circular and linear polarization ratios (ratio of power in the unexpected to the expected polarization) of 1.60 and 0.44; averages of the observations for Europa are 1.56 and 0.47 respectively. We also find by accounting for these additional effects, the original estimates of the reflected power from buried craters were too large. However, the buried crater model still predicts larger echoes than other models that can also account for the polarization ratios. We will compare this model with other models that have been proposed with regard to their correspondence to current data as well as their predictions for other experiments that could be done in the future, such as range mapping. Despite an uncertain geophysical hypothesis, the buried-crater model is distinguished by its ability to simultaneously account for the main features in all the types of data with a minimum of ad hoc assumptions. Finally, by introducing a gradation in refractive index at the crater walls, it is possible to model the sparse data indicating a frequency dependence in the polarization ratios.

Adv. Space Res. Vol. 10, No. 1, (1)195–(1)198, 1990.
Printed in Great Britain.

0273–1177/90 $0.00 + .50

ON THE ANGLE AND WAVELENGTH DEPENDENCIES OF THE RADAR BACKSCATTER FROM THE ICY GALILEAN MOONS OF JUPITER

Eric M. Gurrola and Von R. Eshleman

Center for Radar Astronomy, Stanford University, Stanford, CA 94305, U.S.A.

ABSTRACT

In this paper we report new developments in the buried crater model that has proved successful in explaining the anomalous strengths and polarizations of the radar echoes from the icy Galilean moons of Jupiter – Europa, Ganymede, and Callisto. We have extended the theory to make predictions of the radar cross-sections at all points on the surface of the moon, to compute the shape and strength of the power spectra, and to model a wavelength dependence that has been observed.

DESCRIPTION OF THE MODEL AND ITS THEORY

In /1-3/, Eshleman showed that the huge amplitudes and the unusual polarization properties of the radar echoes from Europa, Ganymede, and Callisto could be explained using a model of buried craters which have a decrease in refractive index at the crater walls. The electromagnetic model involves total internal reflection (TIR) in a geometry that strongly favors backscattering and is similar to the well known optical phenomenon called the glory. This model has some features in common with the surface crater model of Ostro and Pettengill /4/, the random-facet model of Goldstein and Green /5/, and the refraction scattering model of Hagfors, Gold and Ierkic /6/.

In the previous analysis, Eshleman considered the radar properties of a single buried crater at the center of the disc of each moon. This corresponds to $\Theta=0$ in the local crater geometry shown in Figure 1. Also, he did not enter into the complications due to the boundary at the surface of the ice. This interface has a small effect due to the plane wave transmission coefficients which may be obviated by a thin transition zone that matches the impedances of the two media above and below the surface. However, this interface has a more significant effect in defocusing the curved wavefront that is returning to Earth from small coherent glints in the crater. This effect is dependent on the size of the two radii of curvature of the wavefront relative to the depth of the glint. The previous analysis may be considered an upper bound on the model. To bracket the results with a lower bound we have assumed that the glints are deep below the surface so that the emerging wavefronts are spherical when they encounter the interface.

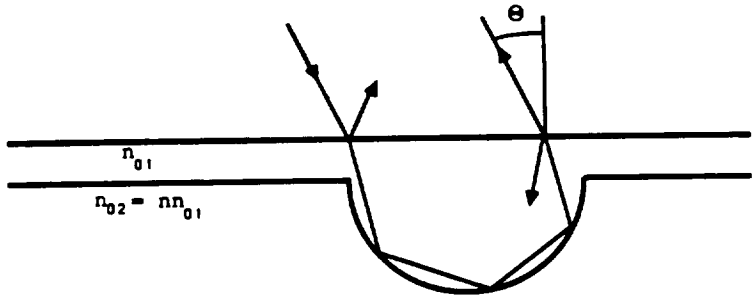

Fig. 1. Geometry of a buried crater and a three-bounce (N=3) ray used in the electromagnetic model. The angle Θ is between the surface normal of the moon and the radar line of sight. For an ice-overburden, $n_{01} = 1.8$. In the model $n_{02} < n_{01}$ (*i.e.*, n<1).

The simplest version of the theory obtains when the moon is assumed to be uniformly covered by identical craters. This may correspond in the actual situation to a uniformity in the average crater properties across the surface of the moon. In that case we can write the normalized (divided by πR^2) cross-sections in the following form :

$$\hat{\sigma}_{SL} = CA(3-x) \ , \ \hat{\sigma}_{OL} = CA(1+x)$$

$$\hat{\sigma}_{SC} = 2CA(1+x) \ , \ \hat{\sigma}_{OC} = 2CA(1-x)$$

$$C = \frac{M\pi r_o^2}{4\pi R^2}\frac{FH}{\lambda}$$

where subscripts L and C refer to linear and circular polarizations; S and O refer to same and orthogonal to the transmitted polarization; M is the total number of buried craters on the surface of the moon; F is the fraction of the central glory circle that is filled by glints; H is the azimuthal size of each glint; r_o and R are the crater radius and the moon radius respectively. The constant C is proportional to the surface density of craters and is used to model the observed radar cross-section of each moon. A and x are complicated integrals of the radar cross-sections of each crater over the surface of the moon. In the theory presented in /1-3/, the mode decoupling factor, x, when TIR occured, was simply the cosine of the product of the number of bounces made by the rays in the crater and the difference in phase between the TE and TM reflection coefficients at the crater walls. In our new theory, x is more complicated in principle. However, numerically the x of the whole moon is virtually the same as the x for a single crater and virtually the same as in the original theory.

The advantage of writing the cross-sections in the above form is that only two independent quantities - CA and x - are required to characterize four quantities - the four radar cross-sections of each moon. If the average crater properties are not sufficiently uniform then this is not possible; the x for the linear cross-sections will differ from the x for the circular cross-sections. Remarkably, the x values inferred separately for linear and circular polarizations indicate that Europa and Ganymede are consistent with the assumption of uniformity.

In /1/, Eshleman noted that a wavelength dependence that has been observed in the relative amounts of power reflected in the orthogonal polarizations could be due entirely to a wavelength dependence in the parameter x. One way that x may be wavelength dependent is if the refractive index at the crater walls makes a smooth transition from n_{o1} to n_{o2}. Here we model the transition zone as a locally planar layer of thickness d with an exponentially decreasing refractive index because this is the simplest profile that admits an analytic solution. (The solution is in terms of Bessel functions whose order depend on $kl\sin\theta$ where l is the scale height of the exponential and θ is the angle of incidence of the rays at the crater wall.)

RESULTS

In the previous papers /1-3/, it was found that x=0.23 is required to achieve a close fit to the observations for all three moons. There are several ways to get x=0.23, but the one that seems most likely is the three-bounce case involving TIR. This requires the hypothesis that n=0.7967. The first three rows of Table 1 compare the observed total radar cross-section and the ratios of the orthogonal components of the circular and linear polarization cross-sections with the predictions of the model. For $\hat{\sigma}$ under the theory column we have used C=1 and given the upper and lower bounds based on the new analysis and the analysis in /1/ respectively.

	Europa	Ganymede		Callisto	Buried craters
	12.6 cm	12.6 cm	3.5 cm	12.6 cm	N=3, n=0.7967, C=1
$\hat{\sigma}$	2.60±0.64	1.52±0.40	1.20±0.28	0.64±0.16	0.67 - 3.6
$\hat{\sigma}_{SC}/\hat{\sigma}_{OC}$	1.56±0.11	1.55±0.06	2.0±0.03	1.19±0.06	1.60
$\hat{\sigma}_{OL}/\hat{\sigma}_{SL}$	0.47±0.07	0.47±0.08		0.55±0.10	0.44
m	1.73±0.08	1.46±0.04		1.43±0.05	1.95
m_{OC}/m_{SC}	1.08±0.10	1.21±0.06		1.13±0.09	0.989

Table 1: The data for the Galilean moons represent averages over many observations and are from Ostro in /7/. $\hat{\sigma} = \hat{\sigma}_{SC} + \hat{\sigma}_{OC} = \hat{\sigma}_{SL} + \hat{\sigma}_{OL}$. m, m_{OC} and m_{SC} are exponents for a least squares fit of the power spectra to a $\cos^m\Theta$ law where Θ is the angle between the radar line of sight and the surface normal of the moon.

In order to match $\hat{\sigma}$ for Europa we require C=3.9 or 0.7 depending on whether the lower or upper bound is used. If FH/λ were 10 (say F=0.5, H=2m, and λ=0.1m), then the buried crater model requires 39% or 7% coverage of the moon's surface by glory craters. Also, note the excellent fit between the polarization ratios for Europa and Ganymede at 12.6cm.

The last two rows of Table 1 characterize the shape of the power spectra in terms of an exponent for a $\cos^m \Theta$ fit to the actual curves. The power in narrow frequency bands is an integration over many craters on lines which are orthogonal to the line of sight and parallel to the spin axis of the moon. The theoretical numbers are based on the new analysis that we have called the lower bound. We don't know yet to what degree the depth of the glints below the surface will affect the shape of the spectra. A comparison between the m values provide new support for the buried crater model. However, they do indicate that the theoretical spectra are narrower than the observed spectra. Also, the m_{oc}/m_{sc} values indicate that the observed OC spectra are a little narrower than the SC spectra while the model has the opposite trend.

It is not clear how precisely a theory needs to match these exponents since the observed power spectra are full of additional structure that is not modelled well by the assumed law. The plots in Figure 2 show typical spectra for Europa, the $\cos^m \Theta$ fit to the data, and the spectra computed for the buried crater model. This clearly shows that a precise fit to m is not necessary to produce simulated spectra that model the data quite well. We also show for comparison simulated spectra for Earth's moon based on empirical formulas determined by Evans /8/, where the SC echo is so weak that it is not visible at the scale shown.

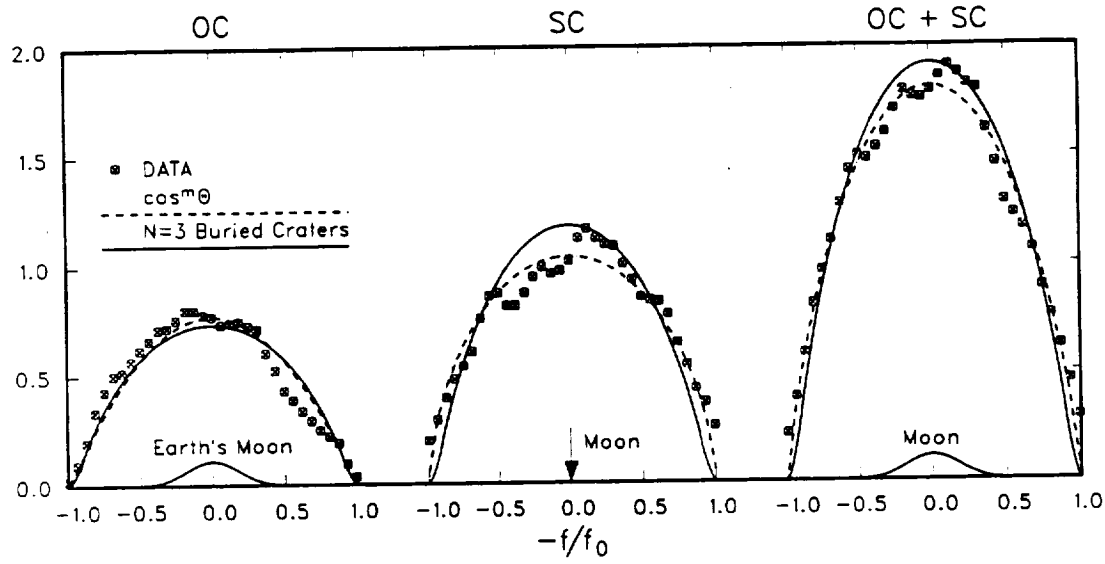

Fig 2. Typical power spectra for circularly polarized waves reflected from Europa compared with the theory and the $\cos^m \Theta$ law. The data are from Ostro /7/ page 221. The exponents for the data(theory) are: m_{oc}=2.14(1.94), m_{sc}=1.22(1.96), and m=1.56(1.95). The data and the theoretical curves have been normalized to $\hat{\sigma}$=2.6; however the $\cos^m \Theta$ curve is not normalized in this manner.

In Table 1 we see that Ganymede has been studied at two wavelengths and that there is a wavelength dependence in these observations. Here, we only consider the dependence indicated for $\hat{\sigma}_{sc}/\hat{\sigma}_{oc}$. To explain the μ_c data for Ganymede, x must go from about 0.22 at λ=12.6 cm to about 0.33 at λ=3.5 cm. Based on the assumption of a gradient in the refractive index at the crater walls as described in the last section, we have computed, in Figure 3, x as a function of d/λ for a single crater at $\Theta = 0$. We have found that the x value of a single crater is very nearly the same as the x value for the entire moon. The 12.6 cm point is determined where x=0.22 and then the 3.5 cm point is determined by the ratio of wavelengths. The x value is seen to increase with decreasing wavelength which is consistent with the data. If this is indeed the cause of the dependence, radar measurements at different λ would be extremely sensitive to the specific subsurface conditions on these moons.

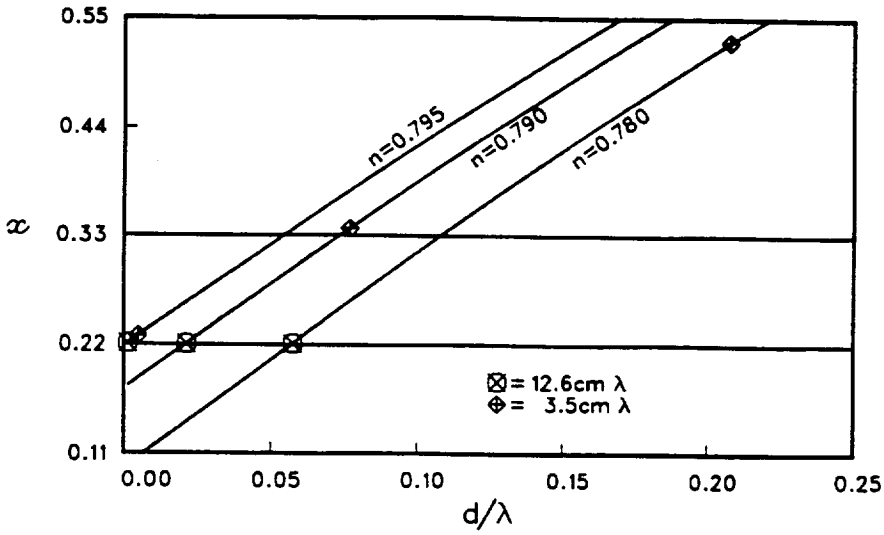

Fig 3. x versus d/λ for three values of n near the optimal value determined for λ=12.6cm.

CONCLUSION

We have demonstrated that the buried crater model is consistent with the anomalous radar characteristics of the Galilean moons. It can explain the surprisingly large cross-sections, the odd reversal of expected polarizations, the broad angular spectrum of the returns, and the apparent change in polarization properties with radar wavelength. More accurate and more discriminating types of radar measurements are needed as further guides for determining the proper theory of the radar echoes from these moons.

ACKNOWLEDGEMENT

This work was supported by the National Aeronautics and Space Administration.

REFERENCES

1. V.R. Eshleman, Radar glory from buried craters on icy moons, Science, 234, 587, (1986).
2. V.R. Eshleman, Mode decoupling during retrorefraction as an explanation for bizarre radar echoes from icy moons, Nature 319, 755, (1986).
3. V.R. Eshleman, The radar-glory theory for icy moons with implications for radar mapping, Advances in Space Research 7.5, 133, (1987).
4. S.J. Ostro and G.H. Pettengill, Icy craters on the Galilean satellites?, Icarus 34, 268, (1978).
5. R.M. Goldstein and R.R. Green, Ganymede: radar surface characteristics, Science 207, 179, (1980).
6. T. Hagfors, T. Gold, H.M. Ierkic, Refraction scattering as origin of the anomalous radar returns of Jupiter's satellites, Nature 315, 637, (1985).
7. S.J. Ostro, Radar properties of Europa, Ganymede, and Callisto, in: Satellites of Jupiter, D. Morrison, Ed., Univ. of Arizona Press, Tucson 1982, p. 213.
8. J.V. Evans, The scattering of radio waves by the moon, Proc. Phys. Soc. B70, 1105, (1957).

Published in the NASA Technical Memoranda, 1991, Planetary Geology and Geophysics Program.

Radar Backscattering by The Icy Galilean Satellites and The Radar Glory Effect.
Eric M. Gurrola and Von R. Eshleman. Center for Radar Astronomy, Stanford University.

Radar echoes from the icy Galilean satellites—Europa, Ganymede, and Callisto—are unique in character, and they may be explained by a phenomenon that has been called the radar glory effect.[1,2,3,4] We have analyzed the radar glory backscattering from buried craters as a possible model for this effect. These craters have a smaller refractive index below the crater than above as shown in Fig. 1(A). The possibility exists that the rays shown will be totally internally reflected at the crater walls, and we assume this to be true in the following. The rays which contribute to the backscattering will come from a circular annulus, when viewed before the refraction occurs at the ice-vacuum surface, in a plane orthogonal to the rays reflected from the crater (see Fig. 1(B)). For craters near the limb of the satellite some of the rays may be blocked by the crater rim, and this circular annulus will break up into two circular arcs. We assume that these glory arcs are broken up into glints of dimension H, assumed larger than the wavelength, and that the fields from a pair of glints connected by the ray shown add coherently while the fields from the various glint pairs add incoherently. The coherent addition of the fields from glint pairs arises because for the ray shown in Fig. 1(A), there is another ray that travels the exact same path, but in the opposite direction.

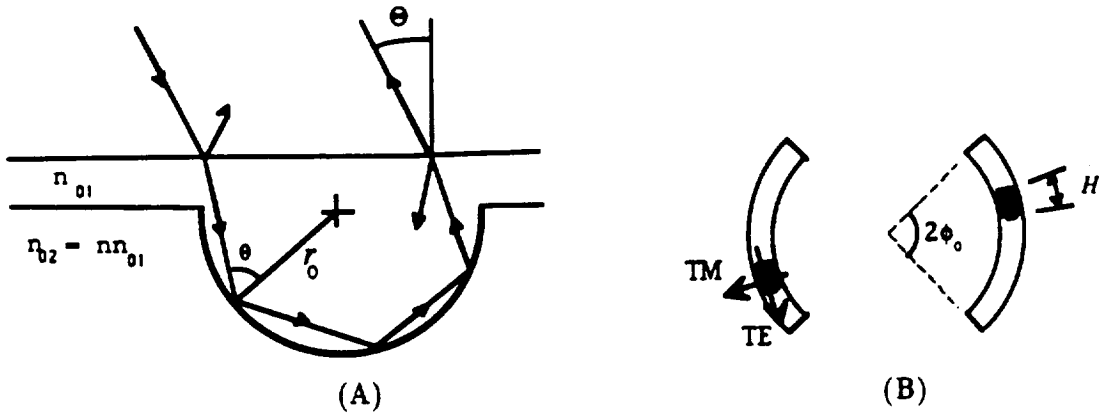

Figure 1. (A) Geometry of a buried crater and a three-bounce (N=3) ray. The angle Θ is between the surface normal of the satellite and the radar line of sight. For an ice-overburden, $n_{01} = 1.8$. In the model $n_{02} < n_{01}$ (*i.e.*, n<1). (B) Glory arcs of angular extent $2\phi_0$ and a pair of glints of dimension H. TE and TM electric field vectors are also shown.

Consider a crater located near the surface of the satellite at coordinates (R, Θ, Φ), where R is the satellite radius, Θ is longitude with $\Theta = 0$ in the direction of Earth, and Φ is latitude with $\Phi = \pi/2$ in the plane defined by the spin axis of the satellite and the $\Theta = 0$ direction. The radar cross-sections for fields received in the orthogonal and same linear (OL and SL respectively) polarizations and those for fields received in the orthogonal and same circular (OC and SC respectively) polarizations are

$$\sigma_{SL}(\Theta,\Phi) = CA_L(3 - X_L) \quad , \quad \sigma_{OL}(\Theta,\Phi) = CA_L(1 + X_L) \tag{1}$$

$$\sigma_{SC}(\Theta) = 2CA_C(1 + X_C) \quad , \quad \sigma_{OC}(\Theta) = 2CA_C(1 - X_C). \tag{2}$$

The constant C is proportional to the number of glint pairs in the glory arcs, and is given by $C = \pi r_o^2 FH/\lambda$ where F is the fraction of the glory arcs filled by glints, H is defined in Fig. 1(B), and λ is the radar wavelength. The A's and X's are given by

$$A_L = \frac{1}{2}\hat{\sigma}_0\{[(T_1^2 + T_2^2) + (T_1^2 - T_2^2)\cos 2(\Phi - \Phi_P)][\phi_0 - (1+x)\delta] + 2T_1T_2(1+x)\delta\} \quad (3)$$

$$\begin{aligned} A_L X_L = \hat{\sigma}_0\{ & 2T_1T_2x\phi_0 \\ & +[(T_1^2 - T_2^2)\cos 2(\Phi - \Phi_P) - (T_1^2 + T_2^2)\cos 4(\Phi - \Phi_P)][\phi_0 - (1+x)\delta] \\ & +2T_1T_2[3(1+x)\delta - x\phi_0]\cos 4(\Phi - \Phi_P)\} \end{aligned} \quad (4)$$

$$A_C = \hat{\sigma}_0\{(T_1^2 + T_2^2)\phi_0 - (T_1 - T_2)^2(1+x)\delta\} \quad (5)$$

$$A_C X_C = 2\hat{\sigma}_0 T_1 T_2 x\phi_0 \quad (6)$$

where

$$\hat{\sigma}_0 = \frac{\sin 2\theta}{N}\frac{\cos^2\Theta}{n_{01}^2\cos^2\Theta'}, \quad (7)$$

$n_{01}\sin\Theta' = \sin\Theta$, Φ_P is the direction of polarization for the linear polarization case, $T_1 = 4n_{01}\cos\Theta\cos\Theta'/(\cos\Theta + n_{01}\cos\Theta')^2$ is the product of the TE Fresnel transmission coefficient for the ray entering the ice and the TE Fresnel transmission coefficient the ray exiting the ice, $T_2 = 4n_{01}\cos\Theta\cos\Theta'/(n_{01}\cos\Theta + \cos\Theta')^2$ is the same product for the TM fields, $x = \cos[2N\tan^{-1}(\cos\theta(\sin^2\theta - n^2)^{1/2}/\sin^2\theta)]$ is the mode decoupling factor defined in reference 1, $\delta = \phi_0/4 - \sin(4\phi_0)/16$, and $\phi_0 = \pi/2$ if no shadowing occurs or $\sin\phi_0 = \cot\theta\cot\Theta'$ when this last definition has a real solution.

The power spectra are sums of the contributions from several craters along lines of constant Doppler shift which are lines, when projected onto the plane of the sky, orthogonal to the line of sight and parallel to the spin axis. That is, the cross-sections at a specified frequency are integrals of the cross-sections in equations (1) and (2) on semi-circles on the satellite surface where $\cos\Theta\cos\Phi$ =constant. In Fig. 2 we compare the computed cross-section for circular polarization with echoes obtained from Eurpoa; this spectrum is typical of the spectra obtained.

The total cross-section of each satellite is an integration of the cross-sections in equations (1) and (2) over the entire illuminated surface. These total cross-sections can be written in a form similar to those in equations (1) and (2) except that the A's and X's are the same for linear and circular polarizations and are complicated integrals that must be computed numerically. In Table 1 we compare a summary of the main features of the data with the model predictions. The scaling constant C for these total cross-sections is given by $C = (M\pi r_0^2/4\pi R^2)(FH/\lambda)$ where M is the total number of craters on the surface.

ACKNOWLEDGEMENTS: This research was supported by NASA grants NGL-05-020-014 and NGT-70056 and NSF grant AST 87-21880.

REFERENCES: [1]Eshleman (1986), *Science* **234**, 587. [2]Eshleman (1986), *Nature* **319**, 755. [3]Eshleman (1987), *Advances in Space Research* **7.5**, 133. [4]Gurrola and Eshleman (1990), *Advances in Space Research* **10.1**, 195. [5]Ostro (1982), chapter 8 in *Satellites of Jupiter*, edited by D. Morrison, University of Arizona Press, Tucson.

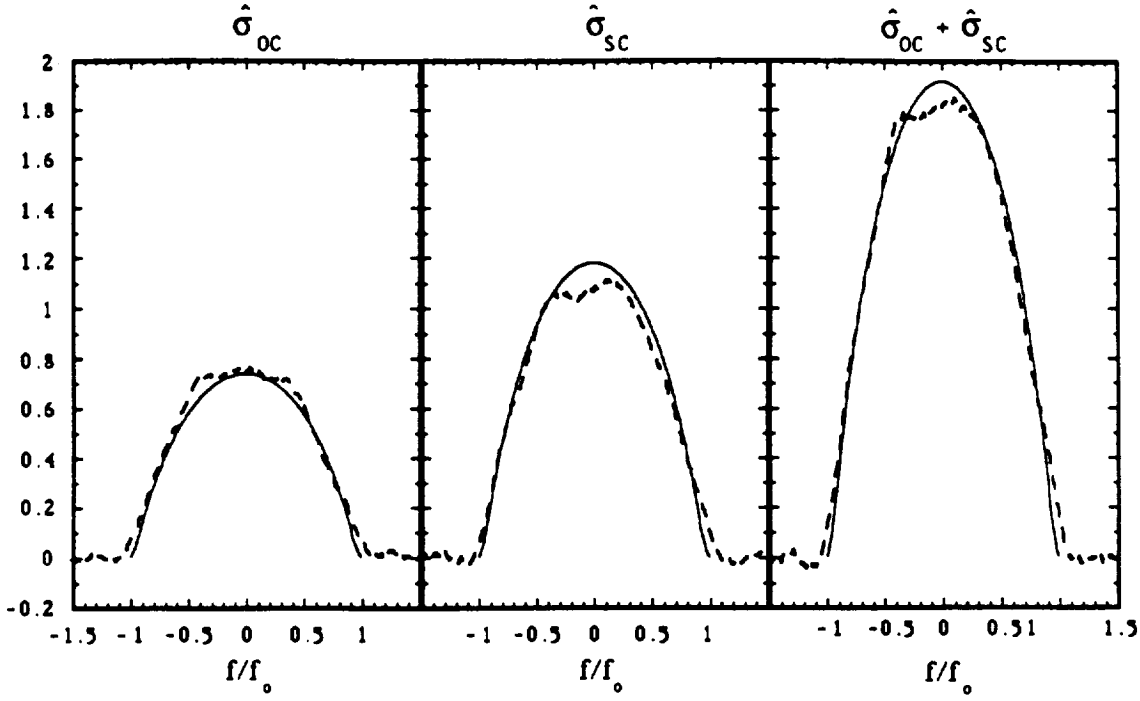

Figure 2. OC, SC, and OC+SC cross-sections obtained from Europa (dashed curves) on January 10, 1990 at the Arecibo Observatory at 12.6 cm-λ and from the model (solid curves) using $N = 3$, n=0.7967. The data and the model have been scaled to give a total cross-section of 2.6.

	Europa	Ganymede	Callisto	Buried craters $N = 3$, n=0.7967, $C = 1$
$\hat{\sigma}$	2.60	1.52	0.64	0.67
$\hat{\sigma}_{SC}/\hat{\sigma}_{OC}$	1.56	1.55	1.19	1.60
$\hat{\sigma}_{OL}/\hat{\sigma}_{SL}$	0.47	0.47	0.55	0.44
m	1.73	1.46	1.43	1.95

Table 1: The data for the Galilean satellites are for 12.6 cm-λ and are from Ostro[5]. $\hat{\sigma} = \hat{\sigma}_{SC} + \hat{\sigma}_{OC} = \hat{\sigma}_{SL} + \hat{\sigma}_{OL}$. These cross-sections are normalized by the geometrical area πR^2, *i.e.*, $\hat{\sigma} = \sigma/\pi R^2$. Here m is the exponent for a least squares fit of the power spectra to a $\cos^m \Theta$ law.